Mesoscale model cloud scheme assessment using satellite observations

Jean-pierre Chaboureau, Jean-pierre Cammas, Patrick J Mascart, Jean-pierre Pinty, Jean-philippe Lafore

Mesoscale model cloud scheme assessment using satellite observations

Jean-Pierre Chaboureau, Jean-Pierre Cammas, Patrick J. Mascart, and Jean-Pierre Pinty
Laboratoire d'Aérologie, Toulouse, France

Jean-Philippe Lafore
Météo-France, Toulouse, France

Received 3 April 2001; revised 20 September 2001; accepted 23 October 2001; published 27 August 2002.

[1] An exploratory evaluation of the explicit cloud scheme of the mesoscale nonhydrostatic (Meso-NH) model has been conducted by comparing synthetic METEOSAT brightness temperatures (BT) to the observed ones. Three different meteorological situations are examined to illustrate the expected degree of accuracy in simulating realistic synthetic BTs in the midlatitude and in the subtropics, with a horizontal grid length ranging from 75 to 12 km. It is shown that the model to satellite approach, which combines the output from a bulk explicit cloud scheme routinely used in mesoscale simulations with a detailed radiative transfer code, offers the possibility of tuning a critical parameter. For instance, tests made with three different values of an ice to snow autoconversion threshold reveal a profound impact on the synthetic BT maps which results in unbiased differences with satellite observations when the appropriate value is selected. The main discrepancies that remain are partly due to errors in the vertical or horizontal placement of the cloud layer or in the amount of condensates, but also due to the lack of subgrid-scale cloudiness in the model. A similar test conducted on the ice water and the liquid water paths confirms the fairly good agreement with retrievals from microwave observations. The paper concludes by discussing the need not only to extend the model to satellite approach to other well-documented cases but also to derive diagnostics from deep convection scheme characteristics in order to include the radiative effect of the convective towers in the generation of synthetic BT maps. *INDEX TERMS:* 3329 Meteorology and Atmospheric Dynamics: Mesoscale meteorology; 3360 Meteorology and Atmospheric Dynamics: Remote sensing; 3354 Meteorology and Atmospheric Dynamics: Precipitation (1854); 0320 Atmospheric Composition and Structure: Cloud physics and chemistry; *KEYWORDS:* mesoscale model, cloud scheme, satellite observation

1. Introduction

[2] Mesoscale models offer an ideal framework for performing detailed and explicit simulations of cloud and precipitation because these models are able to follow the evolution of several microphysical species (cloud droplets and crystals, rain drops, snowflakes, and graupel) in the context of real meteorological flows. The amount, top height, thickness, and precipitation rate of the clouds result from complex interactions between three-dimensional resolved motions and a stratified moist thermodynamical environment. The latter can be highly perturbed locally by the water cycle through the unsteady storage and release of heat and water vapor. Once cloud is formed, however, it is the role of the microphysical scheme to parameterize the physical processes that lead to heat and water transfers between and among the vapor, liquid, and ice water phases. Thus a successful simulation of cloud systems in a mesoscale model outlines at first a geographically and timely accurate prediction of the vertical motions in the atmosphere and then a correct representation of the condensed phase amounts. This makes the objective evaluation of simulated cloud fields against observational data sets, here satellite pictures, so difficult because of the well-known intricate links between small-scale dynamics and the microphysical state of the clouds.

[3] The purpose of this work is to show that a model to satellite approach, in which satellite brightness temperature (BT) images are directly compared to synthetic BTs computed from predicted model fields [e.g., *Morcrette*, 1991; *Roca et al.*, 1997], is helpful in validating mesoscale simulations but since these are already of sufficiently good quality. This method differs substantially from the technique used in model intercomparison exercises defined to evaluate cloud parameterizations [e.g., *Redelsperger et al.*, 2000], where one-dimensional budgets are computed using temporal averages of fine-scale horizontal structures of slowly moving cloud systems in order to show quantitative agreements and to support physical conclusions from the mean vertical profiles. Here the approach is less statistical but more direct in the sense that two-dimensional maps of raw satellite data are used as an absolute reference to assess the correct location and morphology of moving cloud systems,

0148-0227/02/2001JD000714$09.00

Table 1. Model Characteristics

Parameter	Characteristic
Anelastic equations	improved pseudoincompressible approximation
Horizontal resolution	variable following the simulations (see Table 2)
Vertical resolution	51 levels up to 20 km $0 \leq z \leq 8$ km: 60 m $\leq \Delta z \leq$600 m $8 < z \leq 20$ km: Δz =600 m
Vertical coordinate	$\hat{z} = H\,(z - z_s)(H - z_s)^{-1}$ with z usual height, z_s height of topography, H model depth
Physical parameterizations:	
Microphysical scheme	bulk scheme with six prognostic water categories: water vapor, cloud water, rain water, pristine ice, snow, and graupel
Convection	*Kain and Fritsch* [1993] scheme revised by *Bechtold et al.* [2001]
Radiation	European Centre for Medium-Range Weather Forecasts package
Horizontal diffusion	∇^4 operator

a strong issue in the present state of the art of mesoscale modeling. This way of exploiting satellite observations is different from the routine practice in large-scale modeling where comparisons are made on the basis of seasonal mean cloud cover at a relatively coarse horizontal resolution (for example, using measurements from Earth Radiation Budget Experiment [e.g., *Harrison et al.*, 1990]). On the contrary, only a few cases that are well simulated by mesoscale models are candidates for a direct assessment with satellite data because of the rather high accuracy required a priori to predict the cloud location. It is important to stress also that the ''cold start'' procedure used to integrate mesoscale models is dramatic for cloud and precipitation prediction as these are meaningful only after a spin-up period of time.

[4] In a previous study, *Chaboureau et al.* [2000] presented a model to satellite method to evaluate simulations of Fronts and Atlantic Storm-Track Experiment (FASTEX) Intensive Observing Period 17 (IOP17), performed with the mesoscale nonhydrostatic (Meso-NH) model. Synthetic BTs corresponding to the METEOSAT infrared and water vapor channels were computed by a narrowband radiative transfer code. As a result, *Chaboureau et al.* [2000] confirmed that for a midlatitude frontal event a much better agreement between observed and synthetic BTs could be obtained if the cloud scheme included explicitly an ice-phase parameterization. The study revealed also that without specific tuning, the model forecast increasingly overestimated the upper level cloud cover of nonprecipitating ice in the 60-hour forecast range. It is the purpose of this work to understand the recurrent problems of the cloud parameterization and to remedy them by changing a critical ice to snow autoconversion threshold. Owing to its high sensitivity to cloud cover, only information brought by the thermal window (the so-called IR channel of METEOSAT) is necessary to adjust a sensitive coefficient in a satisfactory way. Moreover, the confirmation that the tuning does not deteriorate the hydrometeor content in the mid and lower cloud levels is shown by looking at the ice water path (IWP) and at the liquid water path (LWP), which are simulated by the model and retrieved from microwave observations by two Defense Meteorological Satellite Programme (DMSP) radiometers. This was made possible also because the frontal system that supports the study evolves over the Atlantic ocean, thus providing a simple boundary condition for the satellite data interpretation.

[5] Section 2 presents briefly the Meso-NH model and its cloud parameterization. The computation of satellite radiance from the forecast model variables is then discussed. Section 3 shows the FASTEX IOP17 case of cloud cover simulation that is clearly improved by the model to satellite approach. Model sensitivity to the ice parameterization and comparison with water retrieval from microwave observations are also considered. Section 4 further illustrates the robustness of the tuned cloud parameterization by taking examples from another FASTEX case at higher resolution and a tropical case of the Transport of Chemical Species Across the Subtropical Tropopause (TRACAS) experiment. Finally, section 5 concludes the paper and proposes other tracks where satellite data can be useful to improve mesoscale simulations.

2. Model and Satellite Observations

2.1. Meso-NH and the Simulations

[6] Meso-NH is a nonhydrostatic mesoscale model jointly developed by Météo-France and the Centre National de la Recherche Scientifique (CNRS). A detailed description is given by *Lafore et al.* [1998]. General characteristics of the model, as well as specific parameters chosen for this study, are summarized in Table 1.

[7] In the present model version two explicit cloud parameterizations are available for use in conjunction with the convection parameterization adapted from *Kain and Fritsch* [1993] and revised by *Bechtold et al.* [2001]. The first option parameterizes grid-resolvable warm-rain moisture processes according to *Kessler* [1969] with three prognostic equations for the three-dimensional fields of water vapor, cloud water, and rainwater. The most advanced microphysical scheme is a bulk mixed-phase cloud parameterization developed by *Pinty and Jabouille* [1998] and *Stein et al.* [2000], which predicts the mixing ratio of six atmospheric water categories: water vapor, cloud water, rainwater, nonprecipitating ice, snow, and graupel. Each of the precipitating particles is assumed to follow a generalized gamma function, with mass-diameter and fall velocity-diameter relationships expressed as power laws. The multiple interactions operating between the different water categories are accounted for through the parameterization of 35 microphysical processes (nucleation, conversion, riming, sedimentation, etc.; see *Stein et al.* [2000] for details).

[8] Five numerical experiments are discussed in the subsequent sections (Table 2). Four experiments consider the development of extratropical cyclones sampled during FASTEX, while the other one focuses on a Rossby-wave

Table 2. Summary of the Simulations

Name	Experiment	Resolution, km	Initial Time	Duration, hours	$r_i^\star$, kg kg^{-1}
F1A	FASTEX IOP17	75	1200 UT 17 Feb. 1997	24	5×10^{-4}
F1B	FASTEX IOP17	75	1200 UT 17 Feb. 1997	24	5×10^{-5}
F1C	FASTEX IOP17	75	1200 UT 17 Feb. 1997	24	2×10^{-5}
T	TRACAS	40	0600 UT 29 Nov. 1995	48	2×10^{-5}
F2	FASTEX IOP16	12	0000 UT 17 Feb. 1997	12	2×10^{-5}

breaking episode, part of TRACAS programme. For all of them the fields included in the initial and boundary conditions of the numerical experiments are only temperature, winds, and water vapor. These fields are taken from meteorological model analyses (see below), which did not assimilate any cloud radiance from satellite observations. No cloud initialization of the numerical experiments is performed, i.e., the mixing ratio of the liquid and ice water species build themselves during the course of the simulations. Therefore the assessment of the cloud prediction is meaningful only after a spin-up period that we estimate at 12 hours (see section 3.2).

[9] For the FASTEX IOP17 case the model domain encompasses the North Atlantic sector covering 9000 km × 6000 km on a polar stereographic conformal map projection. The horizontal grid length is coarse, 75 km. Initial conditions and lateral boundary conditions are obtained by interpolation from the operational ARPEGE analyzes of Météo-France [*Courtier et al.*, 1991]. It is initialized on 17 February 1997 at 1200 UTC and is integrated forward for 24 hours. Three simulations (F1A, F1B, and F1C) have been run with $r_i^\star$, a cloud-ice threshold set to different values (see discussion in section 3).

[10] The TRACAS simulation covers 8000 km × 8640 km in the South Atlantic Sector on a Mercator projection at a grid length of 40 km. Initial conditions and lateral boundary conditions are taken from ECMWF analyzes [*Courtier et al.*, 1998]. It is initialized on 29 November 1995 at 0600 UTC and is integrated forward for 48 hours.

[11] The FASTEX IOP 16 case is the result of a two-way grid-nesting simulation [*Stein et al.*, 2000]. The results presented here are from the inner nest, covering 2340 km × 2106 km including the British Isles at a grid length of 12 km. The outer nest has a resolution of 40 km covering 6480 km × 4800 km over the Atlantic Ocean and is initialized by ARPEGE reanalyzes. It is initialized on 17 February 1997 at 0000 UTC and is integrated forward for 12 hours.

2.2. METEOSAT Observations and the Radiative Transfer Code

[12] The IR channel we consider here is in the thermal infrared window (10.5–12.5 μm) of METEOSAT-5. Horizontal resolution is 5 km at the nadir, located at 0°. As the Meso-NH model horizontal resolution is coarser than the METEOSAT resolution, METEOSAT data are averaged and projected onto the Meso-NH grid. At each model grid point the radiance is calculated simply by the average of the METEOSAT data within the grid box.

[13] The radiative transfer code used to simulate the BT is the narrowband version designed by *Morcrette and Fouquart* [1985] and modified by *Roca* [2000]. It has 10 spectral bands unevenly spaced in the IR channel. The radiative transfer code treats clouds as gray bodies with a longwave emissivity depending on the cloud water path, following *Stephens* [1978] for liquid water and following *Smith and Shi* [1992] for ice. Synthetic METEOSAT radiances are derived from fields of temperature, water vapor, liquid water, and ice modeled by Meso-NH. The radiances are computed within the 10 bands simulating the METEOSAT viewing angles. Radiances are then converted to BTs, taking into account the filter function of the IR channel.

2.3. Retrievals of IWP and LWP From Microwave Observations

[14] The retrieval of IWP is based on the 92- and 150-GHz window channels of the SSM/T2 radiometer on board the Sun-synchronous DMSP F12 satellite, following *Liu and Curry* [1996]. The BT depression at 150 GHz is the primary parameter for the IWP retrieval, which is expressed as

$$\beta = (T_{B0} - T_B)/(T_{B0} - 150), \tag{1}$$

where T_B and T_{B0} are the 150-GHz BTs under conditions with and without ice, respectively. Here, T_{B0} is derived from a scatter plot of 92- versus 150-GHz BTs following *Liu and Curry* [1996]. The IWP (in kg m^2), with inclusion of the effect of scanning angle θ is given by

$$\mathrm{IWP} = 3997 \times \beta^{0.79} \cos\theta. \tag{2}$$

As noted by the authors of the method, the IWP retrieved in this way can only be interpreted in a qualitative sense. The BT depression at 150 GHz is due to the scattering by large ice particles, which presumably corresponds to the integrated content of snow and graupel in Meso-NH.

[15] The LWP can be derived from the measurements of the upwelling radiances at 19.35, 22.235, 37.0, and 85.5 GHz, which are measured by the SSM/I imager on board the DMSP series. To illustrate the uncertainty of the retrieval of LWP, we used two different estimates, one using the algorithm of *Weng and Grody* [1994] and another obtained by the method of *Wentz* [1997] for no-rain condition, extending by *Wentz and Spencer* [1998] for the all-weather observations. These methods give the most plausible results according to *Deblonde and Wagneur* [1997], which have found a high correlation between the two techniques, except that the Wentz algorithm gave a LWP 1.75 times larger than by the Weng and Grody method. The LWP provided by the Wentz internet site only represents cloud water (a cloud/rain partition is assumed; see *Wentz and Spencer* [1998]), whereas *Weng and Grody* [1994] indicated that liquid water in the form of raindrops cannot be separated from cloud droplets, so their LWP product includes both categories of liquid water.

3. FASTEX IOP17 Case: Evaluation of the Simulation

[16] As a first example, Figure 1 presents the comparison between observed and simulated BTs, after 24 h of simulation for the FASTEX IOP17 case (F1A experiment). The full-physics Meso-NH configuration used in this run includes the mixed-phase cloud parameterization with the standard settings recommended in *Stein et al.* [2000]. In the mid-Atlantic, the cloud cover of the surface low L41 system (centered near 47°N, 35°W) and the contiguous cloud head (near 45°N, 45°W), as well as the so-called Iceland low (centered near 65°N, 20°W) and its associated cold front crossing Norway (near 68°N, 15°E), are represented by low BTs, less than 250 K, of the same intensities in the two images. However, off the low centers and the frontal areas, the model clearly overestimates the cloud system extent, mostly at upper levels.

3.1. Model Sensitivity to the Ice Parameterization

[17] The upper tropospheric cloud amount in Meso-NH L41 simulation is mainly controlled by a balance between cloud-ice (nonprecipitating) production by water vapor deposition in the ascending area, and cloud-ice destruction by the autoconversion process, which converts (nonprecipitating) cloud ice to (precipitating) snow when some cloud-ice threshold, $r_i^\star$, is reached.

[18] In the current Meso-NH scheme this autoconversion process is parameterized in a heuristic way following *Lin et al.* [1983], using a formula analogous to the cloud droplet autoconversion parameterization that is

$$R_{iauts} = k_{is} \max\left(0, r_i - r_i^\star\right). \quad (3)$$

The inverse time constant k_{is} includes a temperature efficiency factor as in the work of *Lin et al.* [1983], and the critical ice mixing ratio $r_i^\star$ is set equal to 5×10^{-4} kg kg^{-1}. Note that a rather large range of values for the $r_i^\star$ factor can be found in the literature. For example, *Lin et al.* [1983] have set this threshold to 1×10^{-3} kg kg^{-1}, *Rasch and Kristjánsson* [1998] allowed a threshold variation between 4×10^{-4} kg kg^{-1} at 0°C and 5×10^{-6} kg kg^{-1} at −20°C, whereas *Ryan* [2000] adopted a more complicated dependence with cloud type and temperature.

[19] In order to test the sensitivity of the cloud scheme to the process of autoconversion of ice to snow, two additional simulations, F1B and F1C, have been run for the FASTEX IOP17 case with a $r_i^\star$ threshold value set to 5×10^{-5} kg kg^{-1} and 2×10^{-5} kg kg^{-1}, respectively. We first examine a vertical cross-section between (52.80°N, 19.6°W) and (34.8°N, 47.5°W) (see the line in Figure 1) to show the effects of varying $r_i^\star$ on the amounts of nonprecipitating and precipitating ice in the cold and warm front areas.

[20] The vertical structure of the ice mixing ratio appears to be quite sensitive to the $r_i^\star$ value (Figure 2): clouds are denser with a higher threshold. At upper levels, above 10 km, the ice mixing ratio isocontours range from 10^{-5} kg kg^{-1} (for the F1C experiment) to more than 10^{-4} kg kg^{-1} (for the F1A experiment). On the other hand, isocontours of snow greater than 10^{-5} kg kg^{-1} are visible for simulations F1B and F1C but not for the F1A one where snow is absent above 10 km. This means that the cirrus cover is thick in the F1A simulation

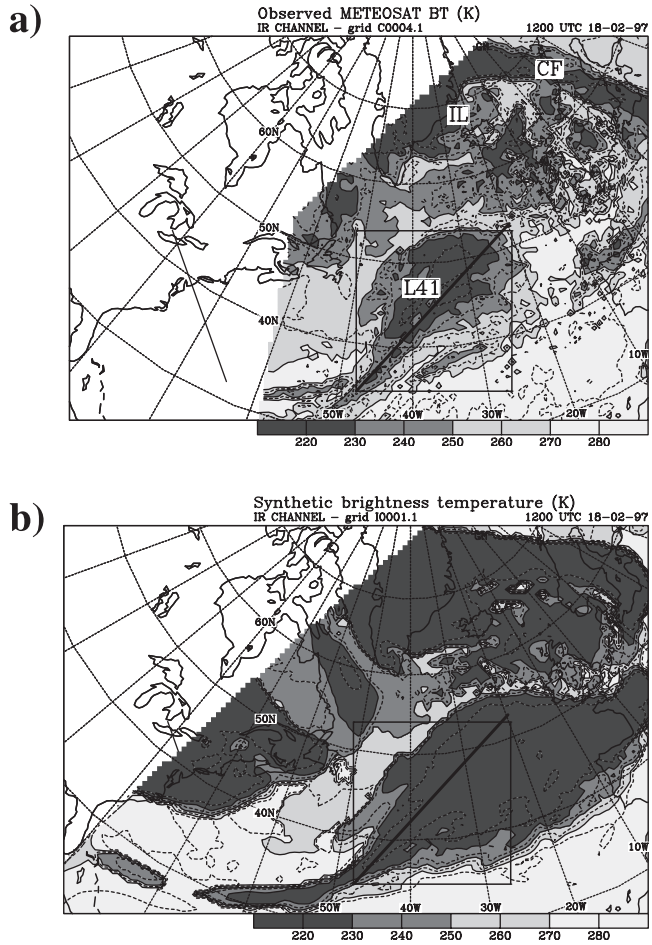

Figure 1. Fronts and Atlantic Storm-Track Experiment (FASTEX) Intensive Observing Period 17 (IOP17) case: (a) observed and (b) simulated brightness temperatures (BTs) (K) at 1200 UTC 18 February 1997, in the IR channel. The BT simulation is F1A (done with the autoconversion threshold set to 5×10^{-4} kg kg^{-1}). Contours are every 10 K alternately dashed and solid. The main synoptic features are marked (L41 for Low 41, IL for Icelandic Low, and CF for Cold Front).

because high $r_i^\star$ prevents a fast conversion of cloud ice to snow that would lead to a partial dissipation of the cirrus by precipitation. At lower levels a higher threshold value also corresponds to denser clouds. However, the area where snow is in excess of 0.3 g kg^{-1} is similar in the three experiments because once formed, the snow crystals grow by collecting small ice crystals at an equivalent rate in the three experiments. So it can be concluded that because the upper level small ice crystals are more sensitive to the choice of the autoconversion threshold, the $r_i^\star$ threshold can be adjusted objectively using BT observations.

3.2. Tuning of the Ice to Snow Autoconversion Threshold

[21] The BTs have been calculated for the three experiments, in order to examine the BT sensitivity to the autoconversion threshold. The results are summarized in Figure 3, which presents the time evolution of the bias and the standard deviation of the difference between the simu-

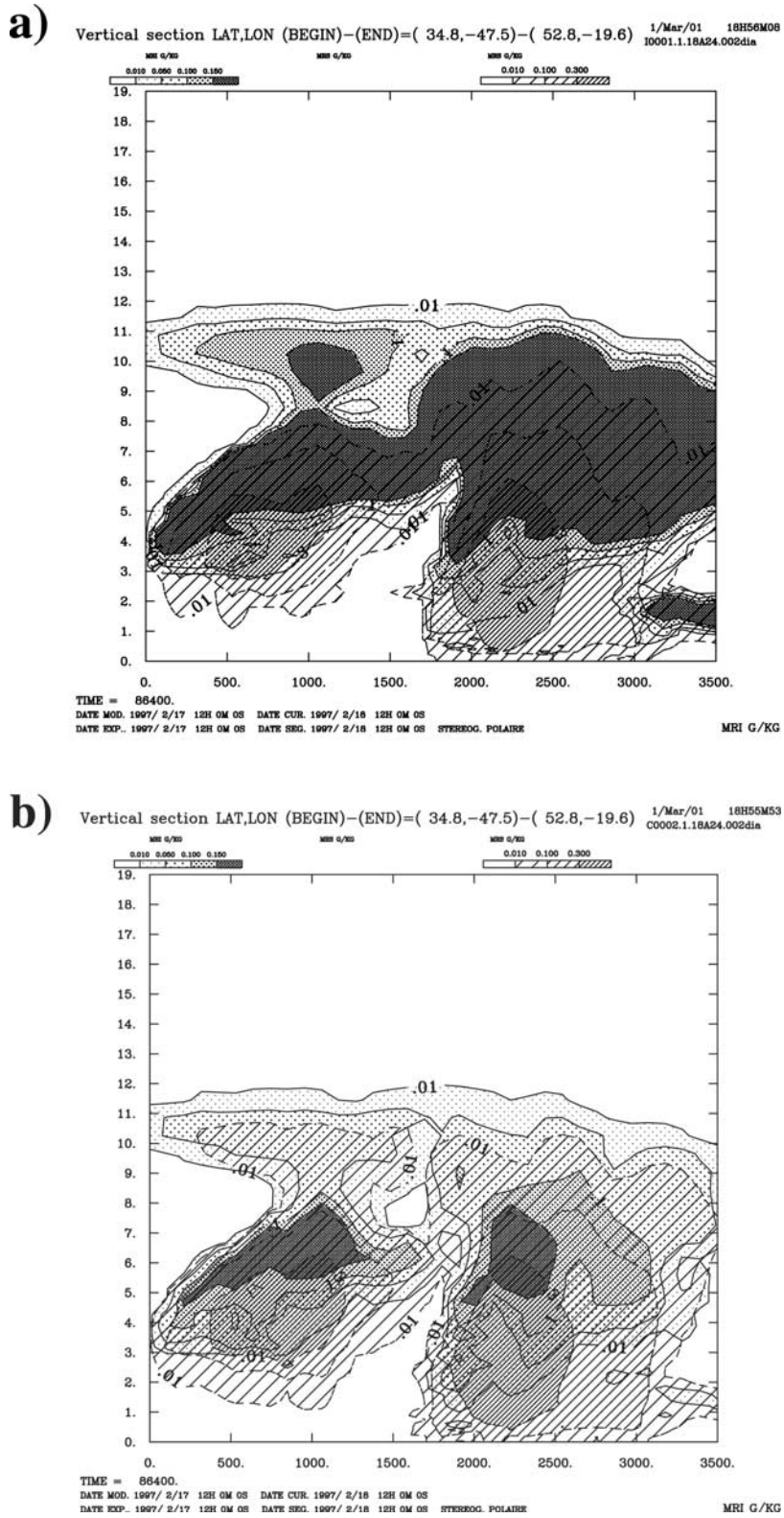

Figure 2. FASTEX IOP17 case at 1200 UTC 18 February 1997. Vertical cross section between (35°N, 47.5°W), left-hand, and (50°N, 20°W), right-hand, of nonprecipitating ice and precipitating ice (snow and graupel) mixing ratios for different threshold values of the ice-to-snow autoconversion (section shown by solid line in Figure 1). (a) $r_i^{\star} = 5 \times 10^{-4}$ kg kg^{-1}, (b) $r_i^{\star} = 5 \times 10^{-5}$ kg kg^{-1}, and (c) $r_i^{\star} = 2 \times 10^{-5}$ kg kg^{-1}. Figures on axis represent distance in kilometers. The solid lines are nonprecipitating ice contours representing 0.01, 0.05, 0.1, and 0.15 g kg^{-1}. The dashed lines are precipitating ice contours representing 0.01, 0.1, and 0.3 g kg^{-1}. The shading are made with dots for the nonprecipitating ice and with hatching for the precipitating ice (the darker the pattern the larger the amount of ice).

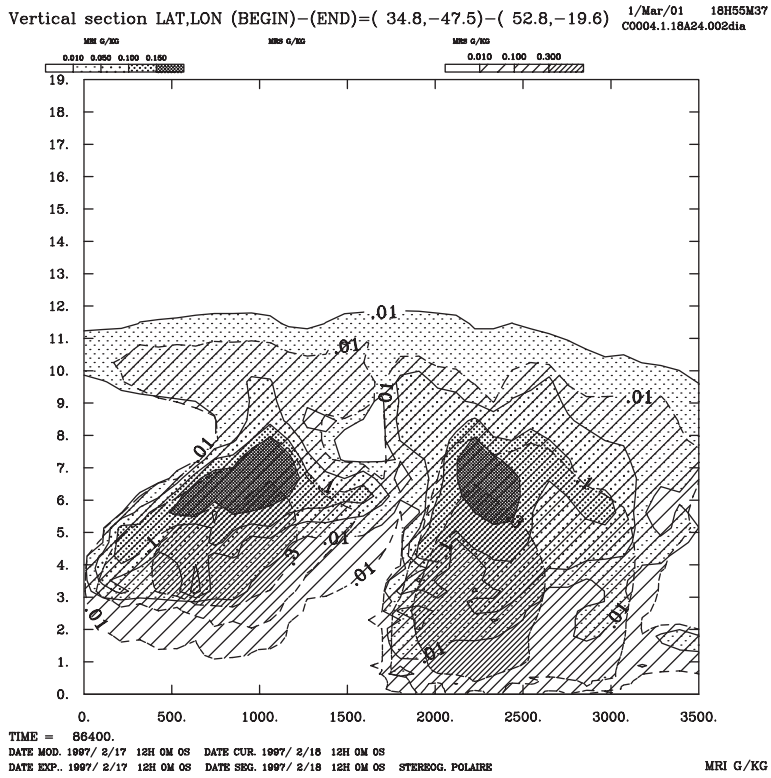

Figure 2. (continued)

lated and the observed BTs for the three sensitivity simulations (calculated over the whole domain where simulation and observation overlap). As there is no cloud initialization in Meso-NH, the bias between METEOSAT and the simulated BTs is the largest at the initial time (17 February at 1200 UTC). Then, as the mixing ratio of the cloud water species build themselves, the bias decreases in time until 18 February at 0000 UTC for the three simulations. After this date and until the end of the simulation the bias either decreases more slowly (F1A) or is steady (F1B and F1C). So this 12-hour initial period corresponds to the model spin up.

[22] With the highest threshold, 5×10^{-4} kg kg^{-1}, the bias between METEOSAT and the simulated BTs decreases in time down to -14 K while the associated standard deviation increases up to 24 K after 24 hours of simulation. As time increases, a larger and larger amount of cloud ice is created, owing to the permanent dynamical forcing, leading to a severely overestimated cloud cover later in the simulation (Figure 1b). So the processes leading to cloud-ice dissipation are underestimated when the autoconversion threshold is too high.

[23] The results obtained with the F1B experiment show that after the spin-up period, the bias, and the standard deviation become steady with smaller values. At the end of the simulation, the bias is negative, around -5 K, and the associated standard deviation reaches 19 K. So clouds tend to have a larger spatial extent (figure not shown). For the F1C experiment the bias becomes negligible after the 12-hour initial period. The standard deviation is also minimum, around 16 K. The latter is twice the precision of the model to satellite approach estimated experimentally by *Chaboureau et al.* [2000].

[24] In order to explain the BT sensitivity to the tuning of the ice parameterization, frequency distributions of BTs are plotted in Figure 4, after 24 hours of simulation, for the gridpoints within the box displayed in Figure 1. The bins are every 5 K. When the threshold is set to 5×10^{-4} kg kg^{-1}, the BT peaks in the intervals between 210 and 220 K with up to 35% of frequency. As shown in Figure 1b, the clouds simulated by F1A have not only a larger spatial extent compared to the observation but are also present at a higher altitude. With a lower autoconversion threshold the frequency distribution shows a more important secondary peak between 250 and 255 K, as is the case for the observed BTs. Thus the frequency distribution of the F1B experiment has a two-peak pattern, but with smaller frequencies at 250 K, compared to the one of the F1C experiment. Finally, the frequency distribution of the observed BTs, which have been averaged within each grid box, appears to be smoother than the one from the F1C experiment. This is partly due to the averaging of the satellite data, but mostly for the warmest BTs (over 250 K) where averaged and nonaveraged (raw) data differ. In particular, the raw observations display a third peak of maximum of BT frequency between 270 and 275 K. These differences reveal the subgrid variability that the model does not take into account because of its coarse horizontal resolution and also because of the possible contribution brought by the embedded convection as discussed in the following section.

[25] We therefore conclude that the F1C experiment displays the best results, particularly in minimizing the bias

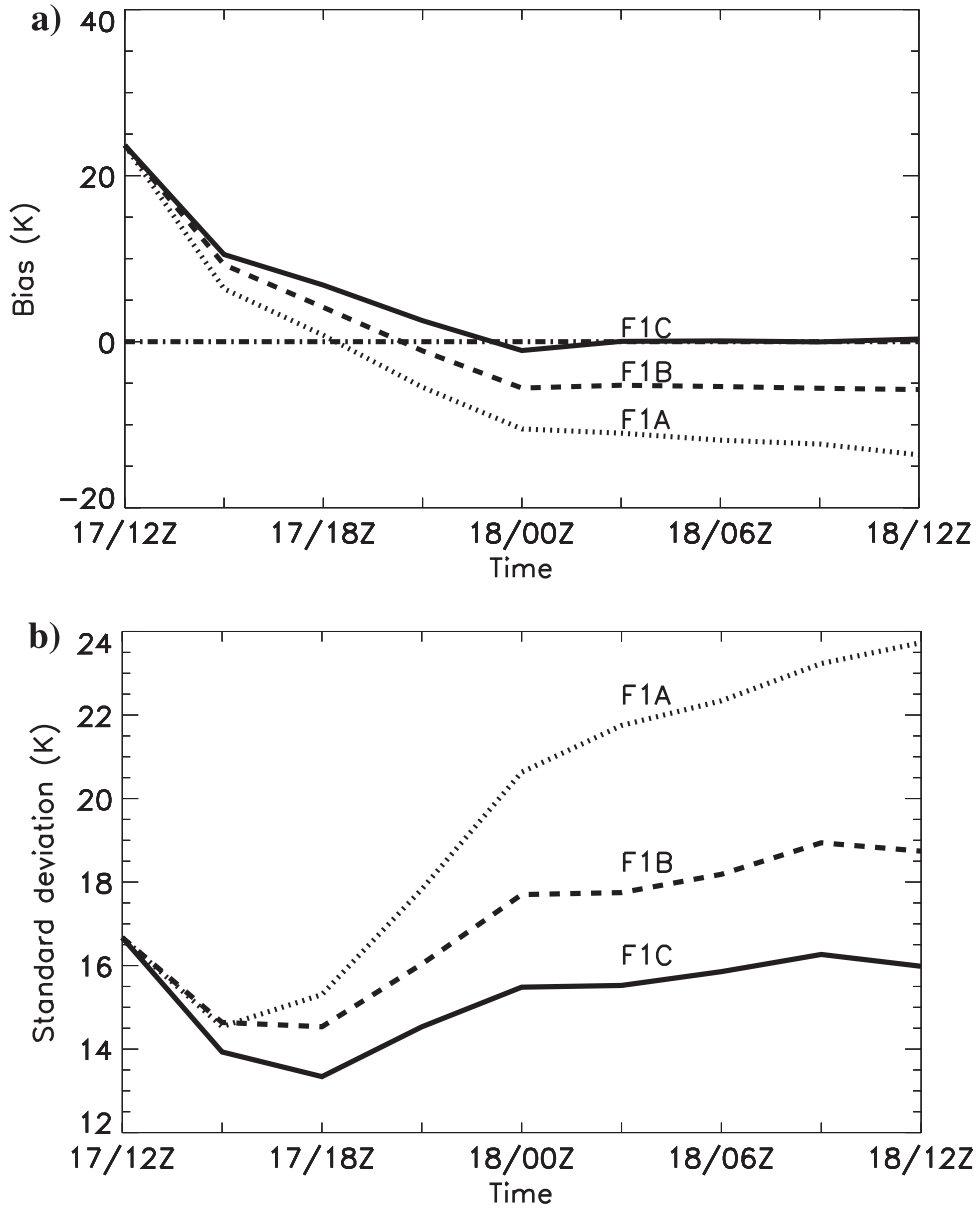

Figure 3. FASTEX IOP17 case. Time evolution of (a) the bias and (b) the standard deviation of the difference between the simulated and the observed BTs (K) in the IR channel for three different simulations (see text). Results are for the period from 1200 UTC 17 February 1997 to 1200 UTC 18 February 1997.

with the observations. Figure 5b presents a map obtained with this new tuning for the simulated BT, after 24 hours of simulation while, for the sake of comparison, Figure 5a reproduces the observation already displayed in Figure 1a. The positioning of the main cloud systems is similar in experiment F1A, F1B (Figure not shown), and F1C, as a result of the strong dynamical organization of the flow that is not very sensitive to details on the ice parameterization at such a scale. The overall cloud cover is much more satisfactory, particularly at the high levels, where the recommended tuning $r_i^\star = 2 \times 10^{-5}$ kg kg^{-1} clearly improves the agreement with the satellite BTs. Nevertheless some discrepancies still remain as highlighted by the BT differences in Figure 6. For example, the shape of the cloud system has a more pronounced stretched structure along the front as compared to the observations. These BT differences on the cloud edges are partly due to the limited quality of the dynamical fields. In particular, the hook shape of the cloud head observed by METEOSAT around 45°N, 45°W results from mesoscale cross-frontal circulations that a simulation of 75-km resolution, i.e., of synoptic scale, cannot fully resolve. Other sources of errors are from the prediction of cloud ice by Meso-NH, whereas the METEOSAT BTs are typical of clear sky (for example, in the area to the east of the box in Figure 6) but presumably also from errors in the vertical placement of the cloud layer or in the amount of condensates. Finally, the lack of subgrid cloudiness in the model leads to the underprediction of small clouds, in

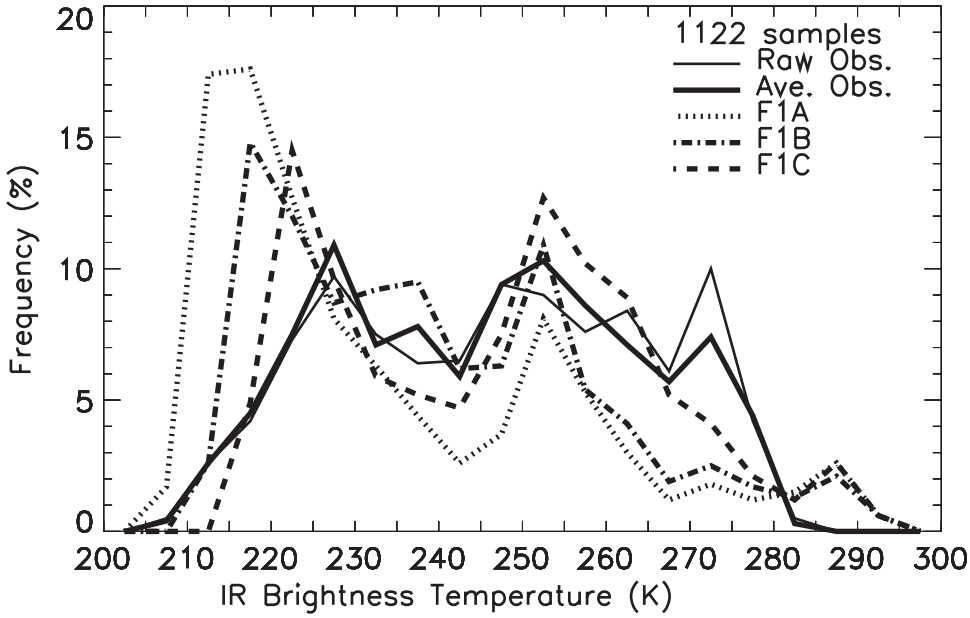

Figure 4. FASTEX IOP17 case. Frequency Distributions of BTs (K) at 1200 UTC 18 February 1997 for grid points within the box displayed in Figure 1. The two solid lines are for the observations, the thickest for the observations averaged within each gridbox and the thinnest for the raw observations (i.e., with no averaging).

particular at low levels probably in the southeastern section of the domain (satellite observations in the visible range confirm such a presence of low clouds; figure not shown). However, large areas indicate BT differences less than 8 K, which are commensurate with our estimate of the error of the model to satellite approach [*Chaboureau et al.*, 2000].

3.3. Physical Significance of the Ice to Snow Autoconversion Threshold

[26] Many experimental studies have been performed recently to characterize the microphysical composition of cold frontal clouds [*Field*, 2000] and high cirrus clouds [*Arnott et al.*, 1994; *Mitchell et al.*, 1996; *McFarquhar and Heysmfield*, 1997; *Platt*, 1997]. All of these agree that a bimodal structure of the ice crystal distribution is often observed even for low cloud temperatures, despite uncertainties in fitting multiprobe measurements. In light of these experimental facts, *Harrington et al.* [1995] developed a double class parameterization which formalizes the partition between the original pristine ice class and a purposely created snow class which collects large vapor-grown crystals of size greater than 125 μm. While other bulk microphysical parameterizations do not include this new ice type category, they must be modified to discriminate between the small and large sized crystals because of their contrasted radiative and aerodynamical properties. Since the present parameterization, like many others, includes a snow/aggregate category of unrimed to lightly rimed crystals, it is legitimate to increase the pristine ice autoconversion rate by simply lowering the $r_i^\star$ threshold in equation (3). Note that the autoconversion term R_{iauts}, the initialization process of snow, identifies crudely the growth of small ice crystals with habit change, owing to self-aggregation and to vapor deposition on the largest ones. Consequently, it seems of no value to consider a sedimentation rate of pristine ice crystals to dissipate cirrus clouds in our simulations as it is often recommended in numerical studies because the snow/aggregate particules are already precipitating. Finally, the snow/aggregate category of ice may also now contain intermediate size crystals at high altitude, a region where self-aggregation process is less efficient. This means that these hydrometeors should be taken into account to compute the cloud radiative properties.

3.4. Sensitivity to the Cloud Radiative Properties

[27] As the radiative properties of ice in clouds are subject to uncertainty, we now test the sensitivity of our synthetic BTs to two other gray body approximations. These differ substantially on the dependence of the emissivity (through the mass absorption coefficient) and its relation to the mean size of the particles (in the following, either r_e the effective radius or the maximum dimension). In the current radiative code, the ice emissivity is parameterized following *Smith and Shi* [1992, hereinafter referred to as SS92], where r_e, varies from 10 μm at 1000 hPa to 40 μm at 100 hPa. This way of determining r_e is the empirical attempt of *Morcrette* [1991] at dealing with the variation of cloud type with height, as smaller water droplets are observed in low-level stratiform clouds, whereas larger particles are found in cumuliform and cirriform clouds. In the last version of the ECMWF model [*Gregory et al.*, 2000] the emissivity is parameterized following Mie theory calculations done by *Ebert and Curry* [1992, hereinafter referred to as EC92]. This parameterization is used with an observationally derived formulation of r_e of *Ou and Liou* [1995], in which r_e increases with temperature, from 25 μm at 210 K to 130 μm at 250 K, the variation usually being attributed to accretion on falling crystals. Another parameterization comes from *Kristjánsson et al.* [1999, hereinafter referred to as KEM99], based on anomalous diffraction theory,

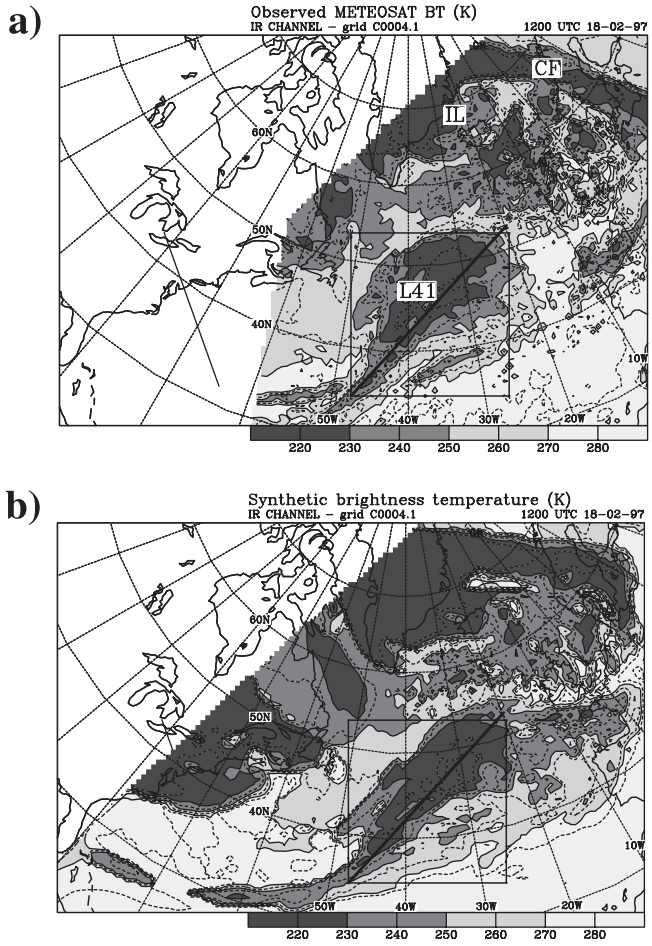

Figure 5. FASTEX IOP17 case: (a) observed and (b) simulated BTs (K) in the IR channel at 1200 UTC 18 February 1997. The BT simulation is F1C (done with the autoconversion threshold set to 2×10^{-5} kg kg^{-1}). Same convention as in Figure 1.

where the size parameter describing the maximum dimension of the ice crystals also increases with temperature, from 25 μm at 210 K to 200 μm at 250 K.

[28] Figure 7 presents the variation of cloud ice emissivity with temperature, obtained from the three parameterizations and for two typical ice paths, 20 and 60 g m^{-2}. (To calculate the SS92 emissivity, we have considered a linear variation of the cloud temperature from 210 K at 100 hPa to 270 K at 1000 hPa.) The parameterizations display similar emissivities at 210 K for the two ice paths, but dramatically different emissivities at 250 K. Thus, when the temperature increases, the emissivity decreases more rapidly with EC92 than with KEM99, whereas the SS92 emissivity increases a bit. Therefore, when applying the two parameterizations to the three simulations (Figure 8), the synthetic BTs obtained with the EC92 emissivity are warmer than those obtained with the KEM99 parameterization, themselves warmer than the BTs using the SS92 scheme. In particular, a bias close to zero is obtained both with the F1C simulation using the SS92 emissivity and with the F1B simulation using the EC92 emissivity. This displays the limitation of tuning the autoconversion threshold but, whatever the radiative parameterization chosen, the synthetic BTs from the F1A simulation are consistently too low compared to the observed BTs. This demonstrates the need of a reduced ice to snow autoconversion threshold as justified in the preceeding section.

[29] Another question arises in the use of these parameterizations. First, the gray body assumption is valid as long as the ice crystals are small compared to the wavelength of the observation. This is questionable as soon as the size exceeds 50 μm or so. Furthermore, as these parameterizations should involve all the categories of ice particles, it is important to test whether the precipitating ice contents (snow and graupel) contribute to the BT calculation. Figure 9 displays the case of including snow in the KEM99 parameterization. In the case of the F1A simulation, no BT change is discernable because the nonprecipitating ice layers are either absorbing too much or the precipitating ice layers are too thin or at too low a level. In the case of simulations F1B and F1C, the addition of snowflakes leads to lower BTs. Thus, for the F1C simulation, a bias close to zero is obtained satisfactorily with either the SS92 emissivity or the KEM99 emissivity (when accounting for the contribution of snow).

3.5. Comparison With IWP Retrievals

[30] The cloud scheme evaluation now goes deeper into the clouds through comparisons between vertically integrated contents of the precipitating ice from Meso-NH and retrievals of IWP from SSM/T2 observations. The observation of IWP is taken around 1200 UTC, and there is almost no temporal lead with respect to the simulation (Figures 10a and 10b). The comparison is limited to the warm front (to the west of 40°W) as the available satellite has flown mostly over this structure. In this area the agreement between the two maps is correct. However, the spatial extent of the IWP ahead of the low is larger in the simulation than in the observation. This is probably related to the more elongated cloud top pattern already noticed in previous section from the BT maps (Figure 5).

[31] Trying to sketch a quantitative comparison, we present a frequency distribution (Figure 10c). The compar-

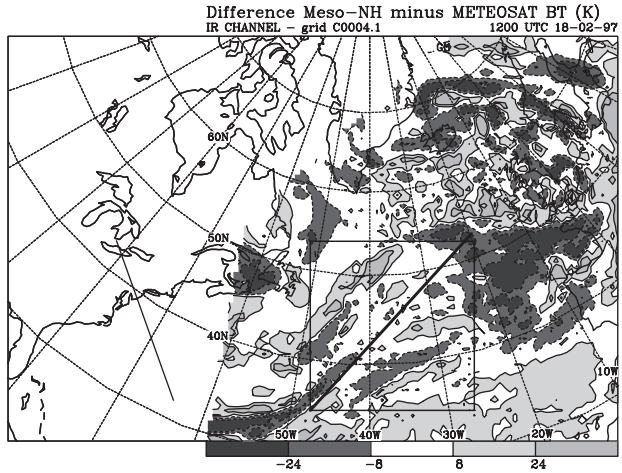

Figure 6. FASTEX IOP17 case: simulated minus observed BTs (K) in the IR channel at 1200 UTC 18 February 1997. The BT simulation is F1C (done with the autoconversion threshold set to 2×10^{-5} kg kg^{-1}). Negative (positive) isocontours are dashed (solid) lines.

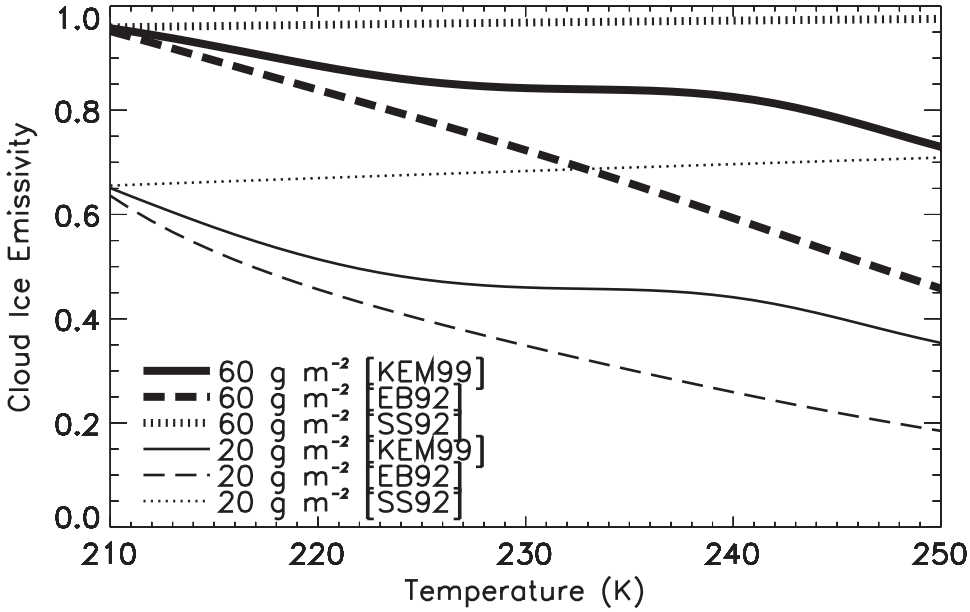

Figure 7. Ice cloud emissivity for three different parameterizations (SS92 [*Smith and Shi*, 1992], EB92 [*Ebert and Curry*, 1992], KEM99 [*Kristjánsson et al.*, 1999]) and for two ice paths (20 and 60 g m^{-2}).

ison is limited to the gridpoints within the box displayed in Figure 10a, and for which both observed and simulated IWPs are nonzero. The bins are every 0.1 kg m^{-2}. First, the frequency distributions from the three experiments are very similar to each other, showing that the column-integrated precipitating-ice value is not sensitive to the autoconversion threshold. So, the slight influence of the ice autoconversion threshold on the IWP distribution is not sensitive enough to allow the tuning of this parameter. Second, despite the warning on the quality of the retrievals given by *Liu and Curry* [1996], the frequency distributions of both the observation and the simulations show similar variations. Finally, the simulations tend to underpredict low to mid IWPs, which may be attributable to the lack of a subgrid cloud scheme in the model.

3.6. Comparison With LWP Retrievals

[32] Our discussion goes further inside the clouds through comparisons between vertically integrated liquid water contents from Meso-NH and retrievals of LWP from

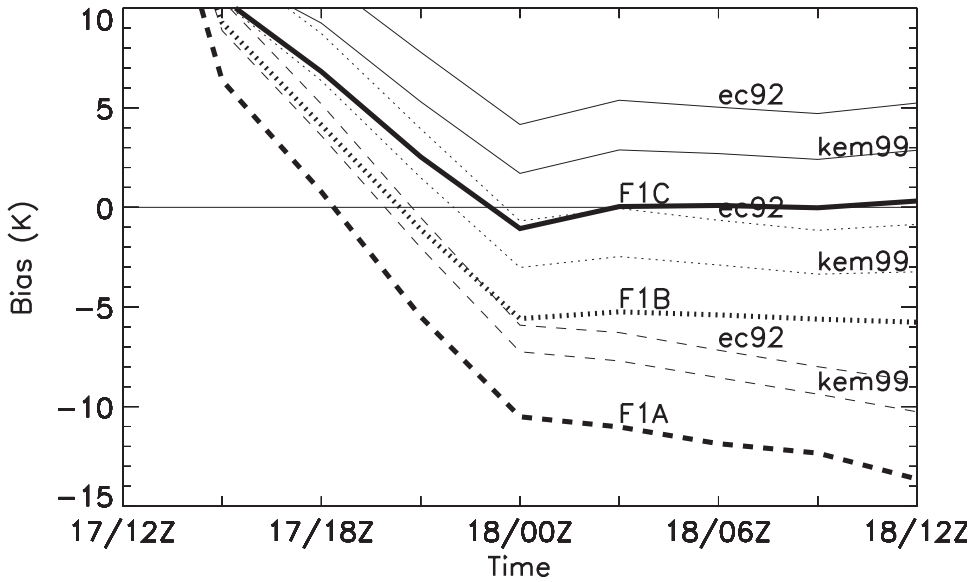

Figure 8. FASTEX IOP17 case. Time evolution of the bias between the simulated and the observed BTs (K) in the IR channel for three different simulations in thick solid line (F1A, F1B, and F1C; same results as in Figure 3a, i.e., using the *Smith and Shi* [1992] parameterizations). In addition, the thin lines are the bias for two other radiative parameterizations of the ice cloud (EB92 [*Ebert and Curry*, 1992] and KEM99 [*Kristjánsson et al.*, 1999]).

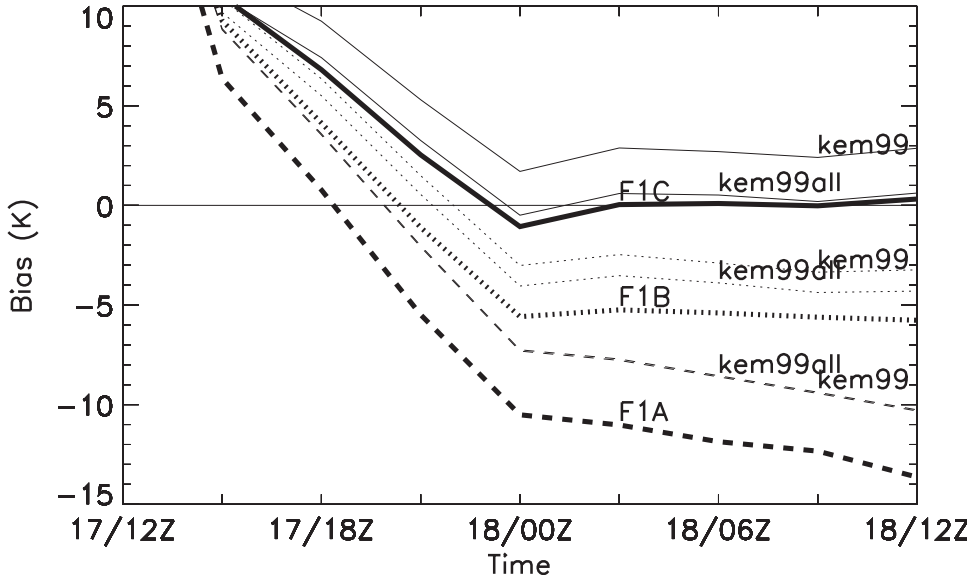

Figure 9. FASTEX IOP17 case. Time evolution of the bias between the simulated and the observed BTs (K) in the IR channel for three different simulations in thick solid line (F1A, F1B, and F1C; same results as in Figure 3a, i.e., using the *Smith and Shi* [1992] parameterizations). In addition, for each simulation, the thin lines are the bias for another radiative parameterization of the ice cloud [*Kristjánsson et al.*, 1999], KEM99: only integrating the ice mixing ratio in the IWP (same results as in Figure 5a) and KEM99ALL: integrating all the ice particle mixing ratios (ice, snow, and graupel) in the IWP.

SSM/I observations. The LWPs calculated from Meso-NH simulations are the column-integrated content of both cloud water and rain like the LWP retrieved by the *Weng and Grody* [1994] algorithm (while the LWP retrieved by the method of *Wentz* [1997] only represents cloud water). Retrievals with the *Wentz* method lead to larger amounts of LWP as compared to those obtained with the *Weng and Grody* algorithm (Figures 11a, 11b, and 11d) and in agreement with the study of *Deblonde and Wagneur* [1997]. The higher LWP values are found in the frontal areas west and east of the surface low (Figure 11a, 11b, and 11c). However, maximum values of LWP are concentrated just north of the low center for the observations, whereas they are continuously present along the warm and cold fronts in the simulation. Note that the ratio of rain to LWP for the simulation is over 20% and even over 40% in the core of the fronts (Figure 11e). The shape of the fronts also shows a more stretched pattern in the simulation. This is consistent with the over-stretched pattern of the simulated IWP and the underestimated low simulated BTs at 1200 UTC, already noticed in the previous sections. Another point of interest is the splitting of the cold front into two parallel fronts to the west of the low center in the simulation, a feature which is also discernable in the observation.

[33] Owing to the temporal lag between the observed and the simulated fronts (the DMSP-F13 satellite swath was taken at 0833 UTC) and to the difference in structure, we analyze the results in the form of frequency distributions (Figure 11d). Here, the comparison is restricted to grid points inside the box displayed in Figure 11a where both observed and simulated LWPs have positive values. The bin width is 0.05 kg m^{-2}. First, one can notice that the frequency distributions are very similar for the three simulations, showing only a weak sensitivity of the autoconversion threshold to the column-integrated variable of liquid water. Second, a large number of small LWP contents, lower than 0.05 kg m^{-2}, is found in the retrievals and the simulations. With such a range of variation, it is difficult to estimate the quality of the cloud scheme. Moreover, and as already discussed in the literature (see, for example, *Deblonde and Wagneur* [1997]), the retrieval algorithms produce widely different results for low values of LWP (less than 0.05 kg m^{-2}). Furthermore, the occurrence of large LWP (larger than 0.90 kg m^{-2}) found in both the Weng and Grody and the Wentz retrievals is less than what we found in our simulations. This may emphasize an overprediction of large LWP by the model, in areas where the ratio of rain is over 40% (Figure 11e). However, similar frequencies are given for these rainy areas by the Wentz retrieval (where it represents only cloud water) and by the Weng and Grody one (where rain and cloud water are added together). At the very least this also leaves the quality of these retrievals questionable. Thus it is not possible to draw a conclusion on the weakness of the Meso-NH cloud scheme or in the uncertainty of the retrieval algorithms. The simulations tend to underpredict low to mid IWPs, regardless of the retrieval method. As already explained for the BT and the IWP comparison, this may be due to the lack of a subgrid cloud scheme in the model. Finally, the slight influence of the ice autoconversion threshold on the LWP distribution is even weaker than it is for the IWP distribution. This means that this parameter not sensitive enough to allow for a better tuning of the LWP and IWP.

4. A Realistic Tuning?

[34] The previous section has shown that, according to the comparison with METEOSAT data, a realistic simula-

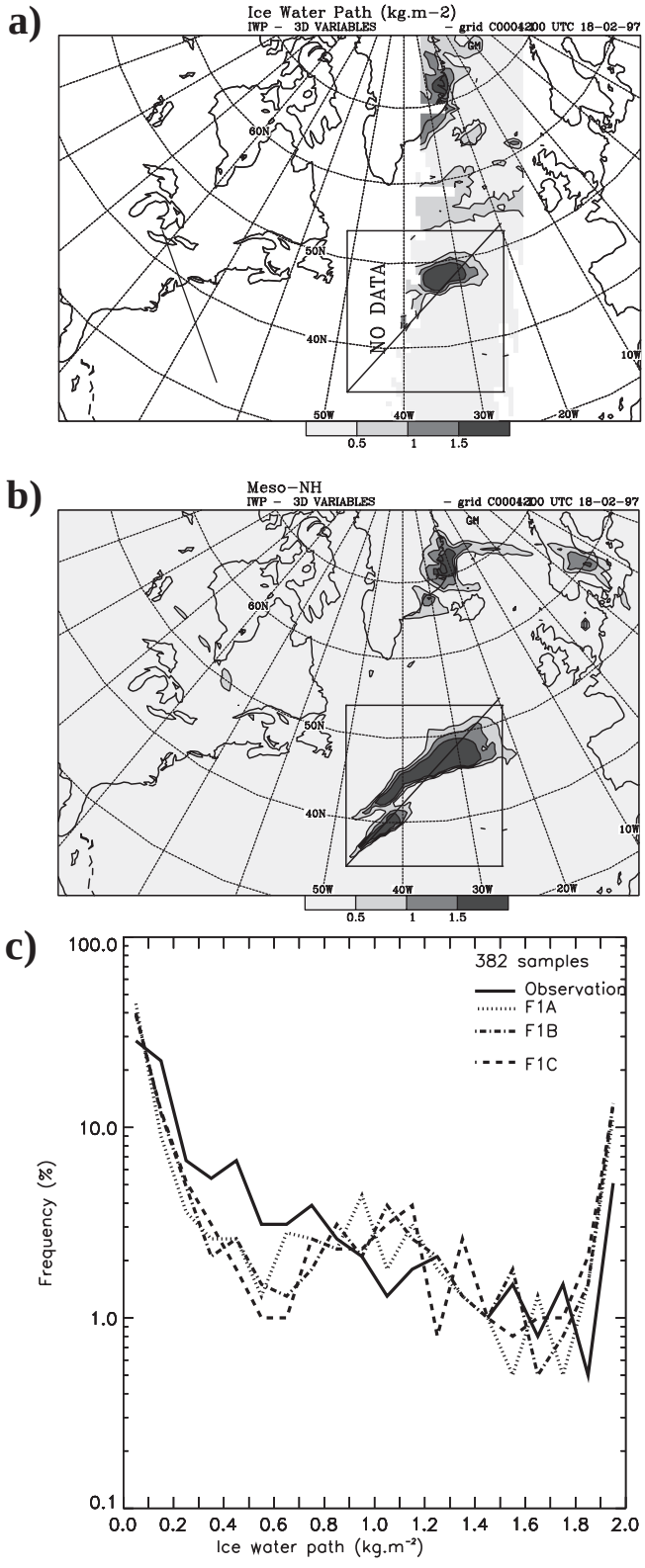

Figure 10. FASTEX IOP17 case: IWP (kg m^{-2}) at 1200 UTC 18 February 1997: (a) observed, (b) simulated (F1C, with the autoconversion threshold set to 2×10^{-5} kg kg^{-1}), and (c) frequency distributions for gridpoints within the box in Figure 10a.

tion of a coarse-resolution midlatitude case can be achieved with the ice-to-snow autoconversion threshold set to 2×10^{-5} kg kg^{-1}. We now investigate the robustness of the cloud parameterization to different conditions, with this new tuning, through two other simulations, a tropical case at a resolution of 40 km and a midlatitude case at a resolution of 12 km.

4.1. Application to a Tropical Case: TRACAS

[35] The TRACAS simulation covers a large domain of the south Atlantic Ocean and thus a wide range of meteorological regimes. Deep convective areas are found along the intertropical convergence zone (ITCZ) just off the equator and over the Brazilian Amazon. The southern part of the domain shows anticyclonic areas with semipermanent low-level stratiform cover west of the Angola coast, and frontal cloud systems in the mid-latitude areas over the southern Atlantic Ocean. The example of BT maps are again chosen at the end of the run, i.e., after 48 hours of simulation (Figures 12a and 12b).

[36] First, it should be noted that the simulation has been run to investigate a stratosphere-troposphere exchange event during a Rossby-wave breaking episode. Therefore this kind of event that occurred in the Subtropics is characterized by a cloud-free area there. Consequently, the cloud systems are located near the boundaries of the domain (which are also the boundaries of the maps in Figure 12). So according to the dominant winds, these cloudy areas might be more controlled by the lateral forcing from the analyses, rather than by the Meso-NH cloud scheme.

[37] In the southern part of the domain two fronts travel eastwards. The associated BTs have similar intensities both in the observation and the simulation, but they are located too far east in the simulation. As for the FASTEX IOP17 case, the cloud systems investigated here largely result from the dynamical forcing. So, these discrepancies in location show that the model dynamics lag the observed atmospheric evolution by roughly 6 hours. On the other hand, the range of BTs indicates that the cloud scheme works correctly to the south of 30°S.

[38] In the ITCZ and over the Amazonian basin the METEOSAT observation shows that deep convection occurs, leading to spots of very low BTs (less than 220 K) surrounded by cirrus shields characterized by BTs less than 240 K. Such intense spots and their associated cirrus shields can be seen in the simulation over land, but not over ocean. For example, some mesoscale convective systems are present in the observation around (5°N, 30°W) and (5°N, 15°W), but not in the simulation. These areas correspond to fully developed deep convective clusters, as a result of a local atmospheric destabilization. These deep convective areas are effectively simulated by the model, both over land and over ocean, as shown by the convective cloud top height in Figure 12d.

[39] This different behavior between land and ocean in the simulation may be tentatively explained by the size of the respective cloud systems, and the way they are simulated. Over land, the convective areas are mesoscale convective clusters which are large with respect to the horizontal resolution of the model (here, 40 km). In these mesoscale convective clusters, the convective vertical trans-

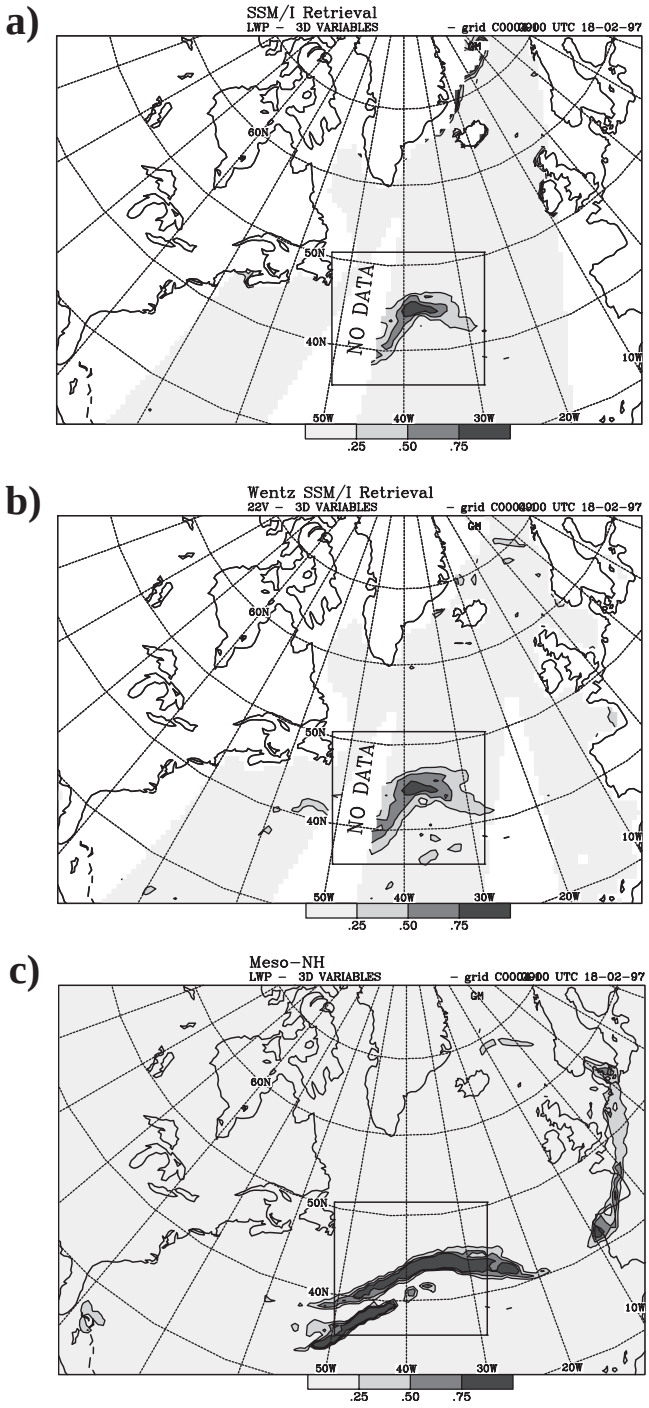

Figure 11. FASTEX IOP17 case: LWP (kg m^{-2}) at 0900 UTC 18 February 1997: (a) LWP retrieved by the *Weng and Grody* [1994] algorithm, (b) LWP retrieved by the method of *Wentz* [1997], (c) simulated LWP (F1C, with the autoconversion threshold set to 2×10^{-5} kg kg^{-1}). (d) Frequency distributions for gridpoints within the box in Figure 11a, and (e) ratio of rain to LWP (in percent) expressed for simulated LWP values over 0.25 kg m^{-2}.

port of moisture is large enough to produce significant cloud water (or cloud ice) detrainment in the upper troposphere, leading to significant resolved water (or ice) mixing ratios in the upper troposphere. The significant values of resolved water (or ice) concentrations therefore show up as cold spots in the synthetic BTs (see, for example, the area to the west of 50°W and between 10°S and 20°S). Over ocean, Figure 12d shows a more spotty convective organization, with cloud top height exceeding 12 km, leading to weaker cloud water (or ice) detrainment in the upper troposphere. The resulting resolved cloud water (or ice) concentrations in the upper troposphere is therefore too small to significantly show up on the synthetic BTs, leading to larger BT differences with the observations.

4.2. Sensitivity to Horizontal Resolution: FASTEX IOP 16

[40] To conclude this set of comparisons, we now examine a much higher-resolution experiment, also selected from the FASTEX studies. Examining the horizontal resolution is a possible issue in the present work as the modeled cloud cover is rather sensitive to the model grid mesh. With coarse resolution, explicit (resolved) cloud are mostly produced in

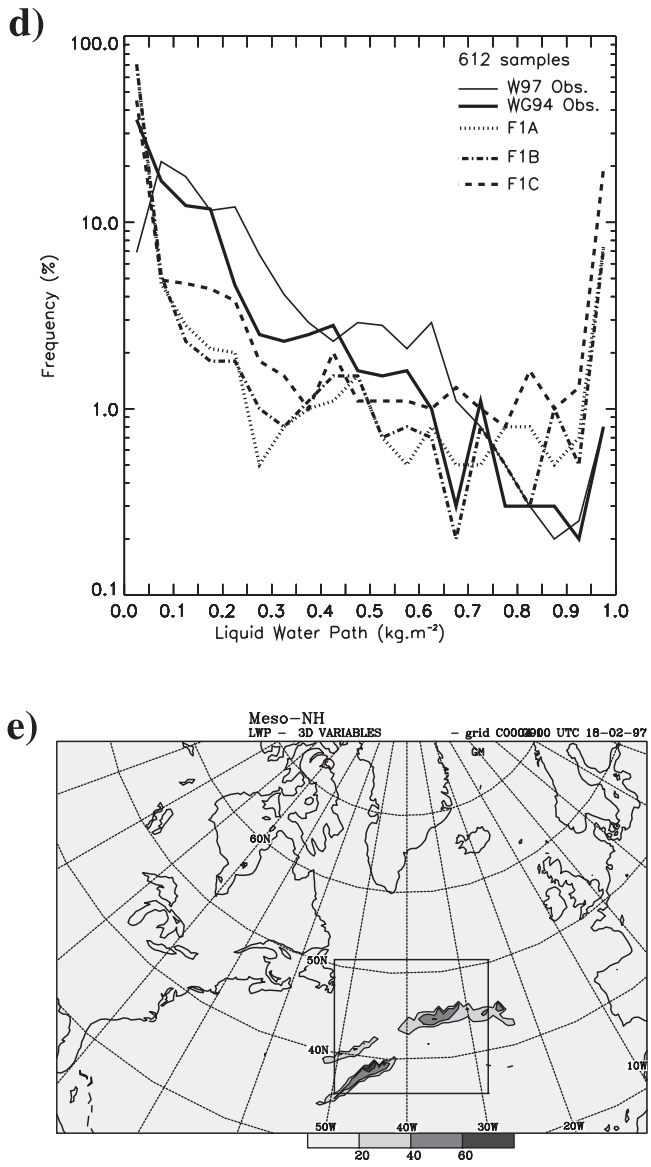

Figure 11. (continued)

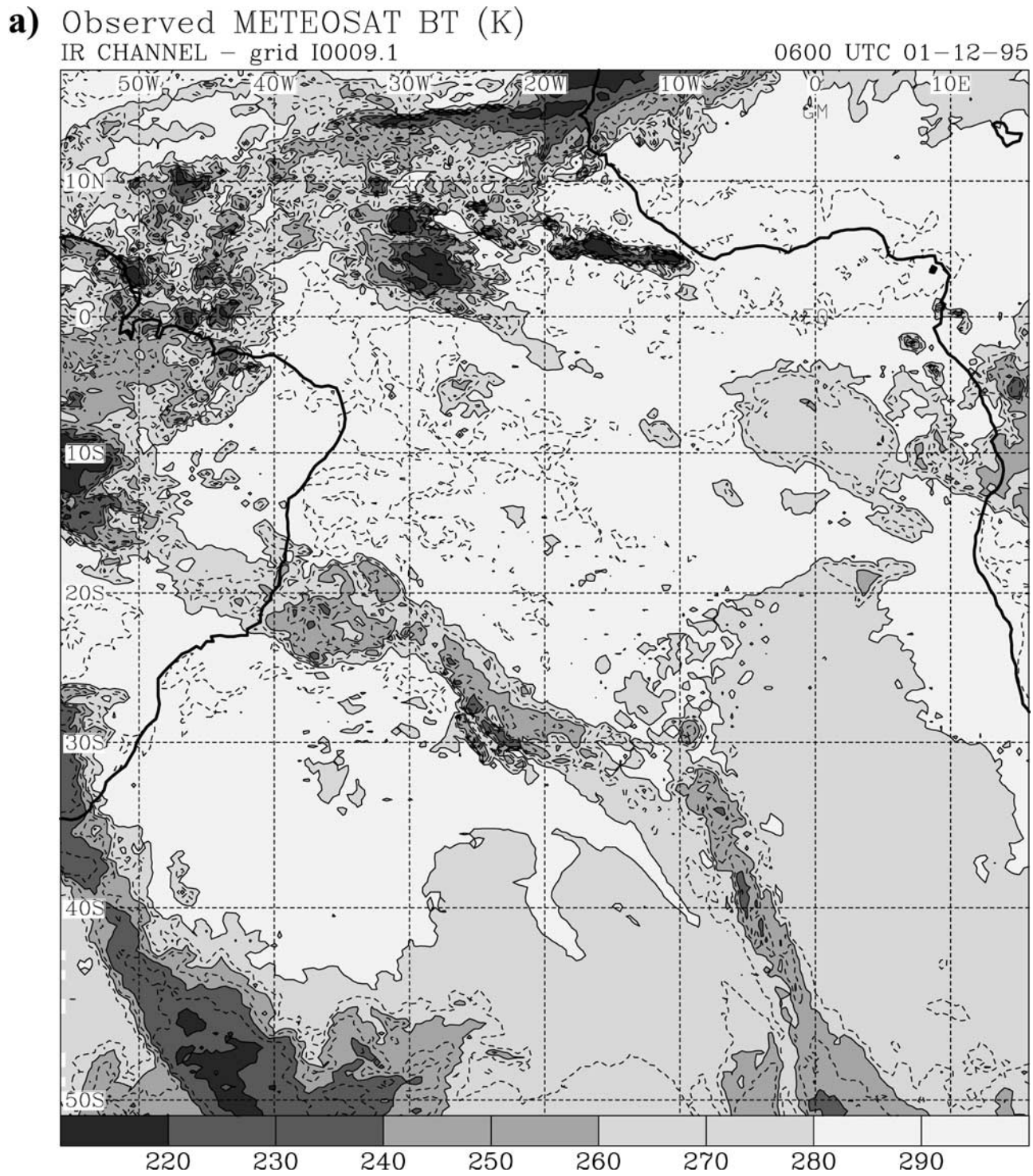

Figure 12. TRACAS case: BTs (K) in the IR channel (same convention as in Figures 1 and 6) and simulated cloud top height (in kilometers) at 0600 UTC 1 December 1995.

frontal and central storm areas, whereas the convective scheme provides extensive cloud cover in other areas. Thus the condensed water distribution produced by the convective scheme is not accounted for in the model to satellite approach. Indeed, the amount of condensed water depends on the updraft mass flux which covers a small portion of the grid, typically less than 5%. Therefore this amount is small, and as soon as the water condenses it evaporates. With high resolution, ~20 km or better, a larger fraction of the cloud cover is produced by resolved condensation, and the role of the convective scheme is reduced. Therefore we might expect a different result from the present model to satellite approach. The FASTEX IOP 16 case gives us an example of the synthetic BT quality at higher horizontal resolution, here 12 km. Also, this resolution is getting closer to the METEOSAT one at midlatitudes, around 7.5 km.

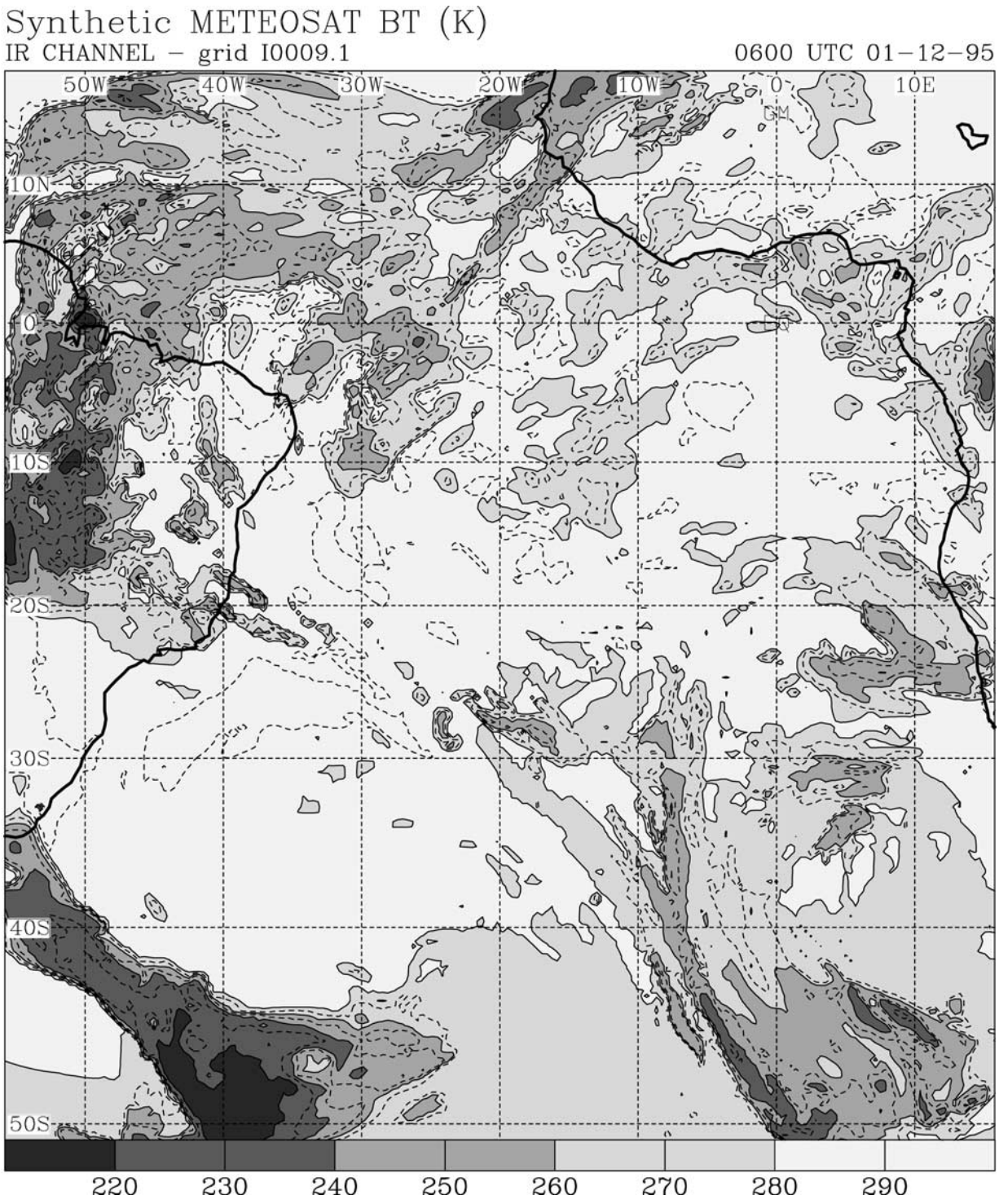

Figure 12. (continued)

[41] Once again, observation and simulation of METEOSAT BT look similar to each other (Figure 13). The principal patterns of cloud cover over the cold front are well represented by low BTs (less than 230 K) to the west of 10°W, while the cloud cover over the warm front is to the east of this line. However, the simulated cloud head (58°N, 15°W) seems detached from the low, compared to the observation. This is largely due to the strength of the dry intrusion, a topic under dynamical investigation. In the cold sector (the upper left quarter of the Figures 13a and 13b), the simulated BTs are larger than the observed ones. As for the TRACAS case in the ITCZ over the Atlantic, the convective processes which occur do not produce enough resolved explicit water condensate. Therefore the convective clouds are underestimated in the simulated BTs. Finally, the cloud cover quality predicted by the present model to satellite technique is not significantly modified when obtained at the model resolution of 12 or 75 km, but this

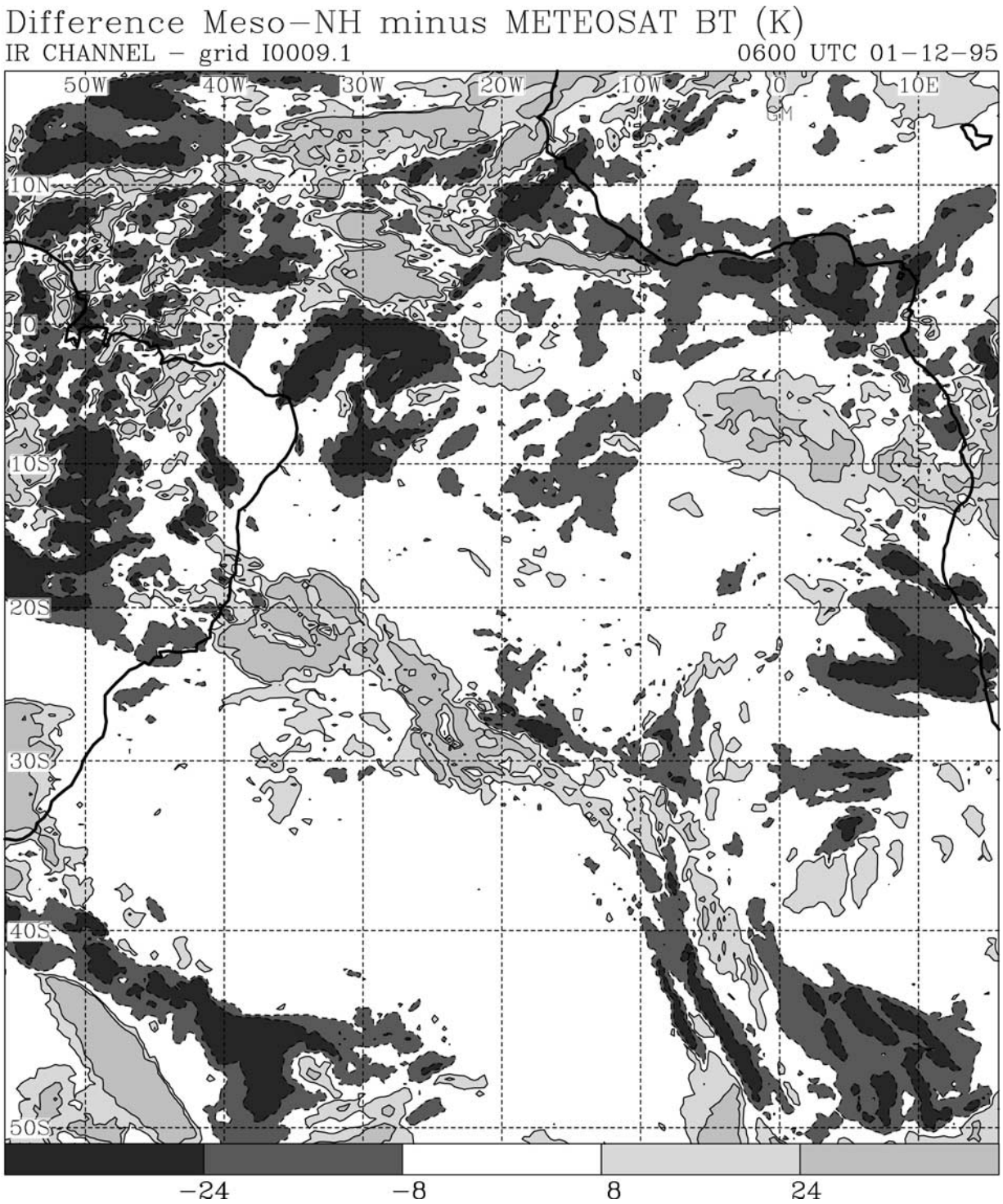

Figure 12. (continued)

statement probably has to be confirmed on a wider set of case studies.

5. Conclusion

[42] An evaluation of the cloud scheme of the Meso-NH model has been made by comparing synthetic and observed METEOSAT BTs. For three different cases, it has been shown that the model is able to simulate realistic synthetic BTs, both in the midlatitudes and in the subtropics, with horizontal resolution ranging from 75 km to 12 km. Moreover, this model to satellite approach, which combines an explicit cloud scheme implemented in a mesoscale model with a detailed radiative transfer code, allows an examination of the ice parameterization. A comparison made with three different values of the ice to snow autoconversion threshold shows a significant improvement of the synthetic BTs and thus a minimization of the difference between

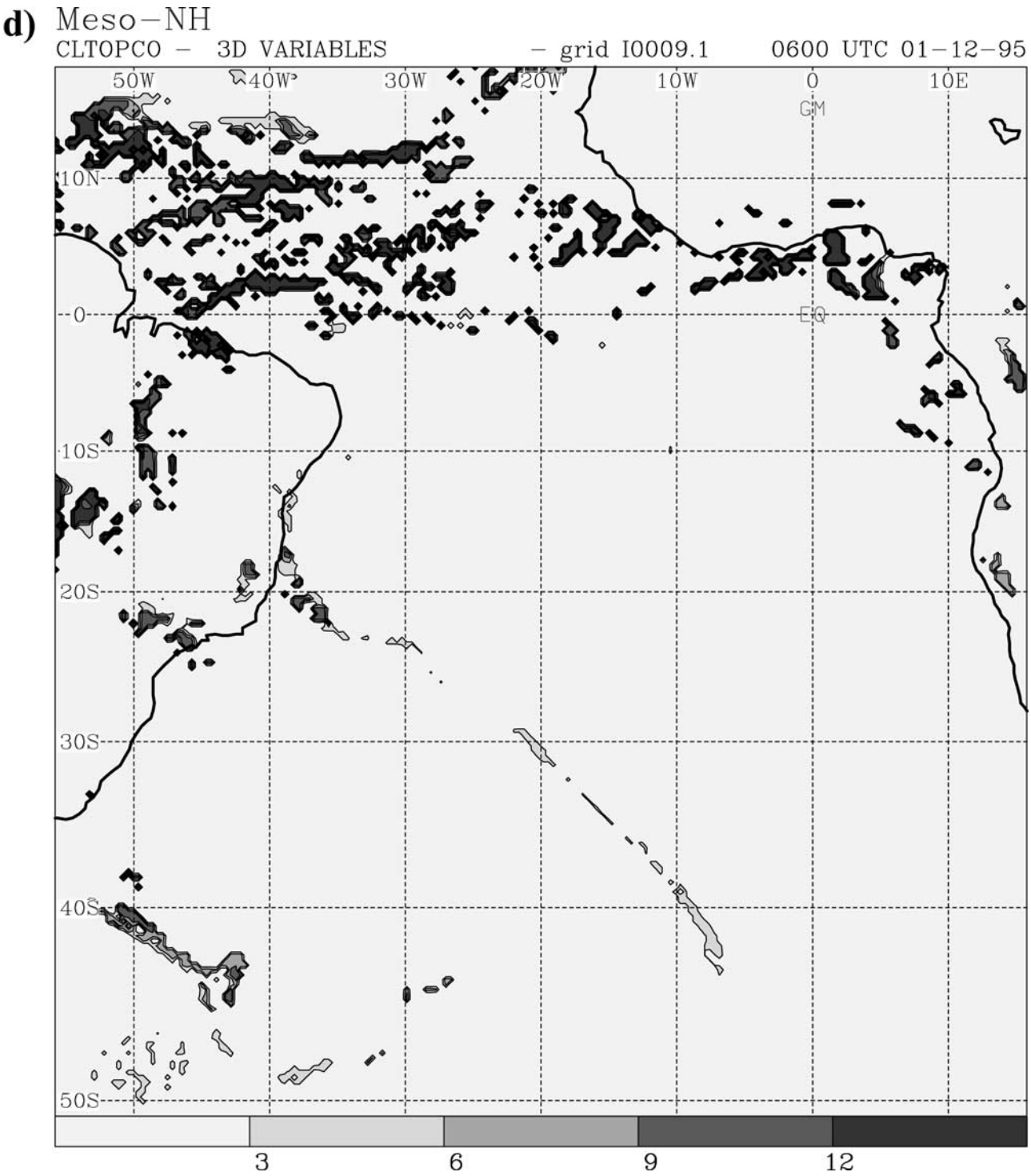

Figure 12. (continued)

simulated and observed BTs. The main discrepancies that remain are partly due to errors in the vertical or horizontal placement of the cloud layer or in the amount of condensates, but also due to the lack of subgrid-scale cloudiness in the model.

[43] A similar test conducted on the ice water path and the liquid water path shows a qualitative agreement with retrievals from both the SSM/T2 and SSM/I observations, regardless of the autoconversion threshold chosen. Some discrepancies were related to the overprediction of low contents and vice versa, but the uncertainties in the retrieval quantities do not allow further interpretation. The use of a full microwave radiative transfer code would presumably lead to a more conclusive test.

[44] The useful reduction of ice to snow autoconversion threshold is interpreted by the presence of bimodal dis-

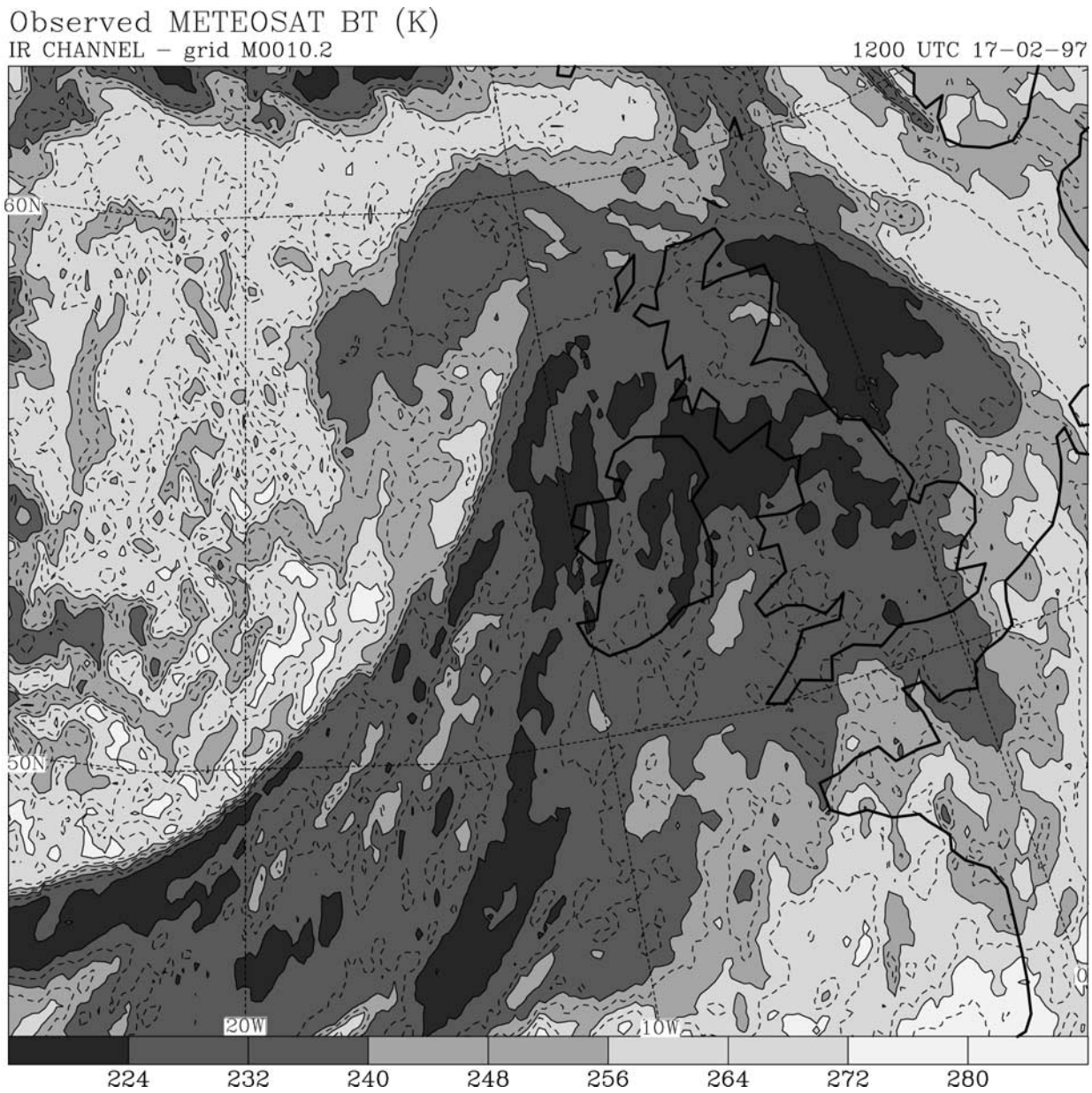

Figure 13. FASTEX IOP16 case: (a) observed and (b) simulated BTs (K) in the IR channel at 1200 UTC 17 February 1997. Contours are every 8 K alternately dashed and solid.

tributions of ice at high altitude as observed extensively in cirrus clouds [e.g., *Mitchell et al.*, 1996]. In addition, the results have been tested with respect to the uncertainty to the radiative properties of ice in clouds. No matter what radiative parameterization is chosen, the simulation with the largest threshold underestimates the BTs. The best tuning of the autoconversion threshold depends upon the choice made in the BT calculation. In this respect, we recommend incorporating the snow/aggregate category of ice in the BT calculation with the KEM99 parameterization.

[45] More generally, parameterizations of the cloud water cycle and of the radiative properties of cloud particles contain implicit assumptions about the number and the geometry of the particles. Recent schemes have been tested to treat the microphysical and the radiative aspects in a consistent way [e.g., *Ryan*, 2000]. The model to satellite technique is also sensitive to these two aspects while keeping in mind the errors arising from the simulated dynamical fields. It is hoped that a multifrequency approach and more experience gained by testing the model to satellite technique on a large set of cases will reduce the uncertainties in the characteristics of the high-level ice clouds.

[46] Finally, the present technique, which only relies on the indirect effect of deep convection through resolved cloud water (and ice) mixing ratio variation, poorly predicts cloud cover itself in areas where large-scale forcing and organizations are weak. Improving our approach along this line is the subject of an ongoing work, where the use of a subgrid cloud parameterization scheme reduces the disagreement between observations and simulations [*Chaboureau and Bechtold*, 2002].

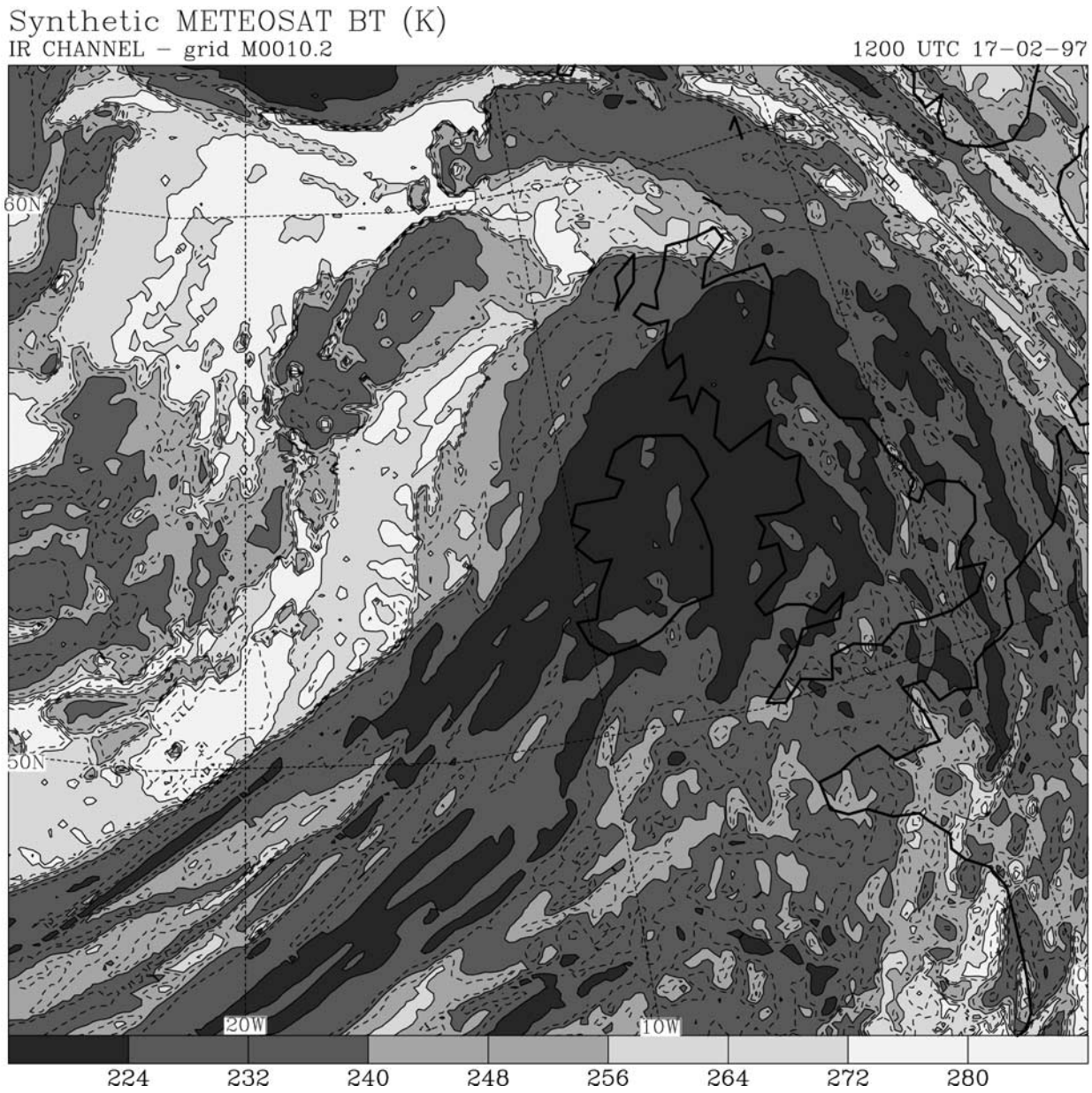

Figure 13. (continued)

[47] **Acknowledgments.** This research was supported by the FASTEX-Cloud System Study Project funded by the European Commission under the contract ENV4-CT97-0625. Computer resources were allocated by IDRIS (projects 97569, 98569, and 981076), and by Météo–France. METEOSAT data are "Copyright EUMETSAT." The SSM/I and SSM/T2 data come from the NOAA Satellite Active Archive. LWP retrievals from the Wentz and Spencer's algorithm are produced by Remote Sensing Systems and sponsored, in part, by NASA's Earth Science Information Partnerships (ESIP): a federation of information sites for Earth science; and by the NOAA/NASA Pathfinder Program for early EOS products; principal investigator: Frank Wentz. The authors would like to thank Rémy Roca and Jean-Jacques Morcrette for providing us with the radiative transfer code. The first author thanks Catherine Prigent for useful discussions on the quality of the microwave retrievals. We are grateful to the anonymous reviewers for the constructive comments that considerably improves the paper and to Robert Rogers for improving the English.

References

Arnott, W. P., Y. Dong, J. Hallett, and M. R. Poellot, Role of small ice crystals in radiative properties of cirrus: A case study, FIRE II, November 22, 1991, *J. Geophys. Res.*, *99*, 1371–1381, 1994.

Bechtold, P., E. Bazile, F. Guichard, P. Mascart, and E. Richard, A mass flux convection scheme for regional and global models, *Q. J. R. Meteorol. Soc.*, *127*, 869–886, 2001.

Chaboureau, J.-P., J.-P. Cammas, P. Mascart, J.-P. Pinty, C. Claud, R. Roca, and J.-J. Morcrette, Evaluation of a cloud system life-cycle simulated by Meso-NH during FASTEX using METEOSAT radiances and TOVS-3I cloud retrievals, *Q. J. R. Meteorol. Soc.*, *126*, 1735–1750, 2000.

Chaboureau, J.-P., and P. Bechtold, A simple cloud parameterization derived from cloud resolving model data: Diagnostic and prognostic applications, *J. Atmos. Sci.*, *59*, 2362–2372, 2002.

Courtier, P., C. Freydier, J.-F. Geleyn, F. Rabier, and M. Rochas, The ARPEGE Project at Météo-France, *ECMWF Sem. Proc.*, *7*, 193–231, 1991.

Courtier, P., E. Andersson, W. Heckley, J. Pailleux, D. Vasiljević, M. Hamrud, A. Hollingsworth, F. Rabier, and M. Fisher, The ECMWF implementation of three-dimensional variational assimilation (3D-Var), *I, Formulation, Q. J. R. Meteorol. Soc.*, *124*, 1783–1807, 1998.

Deblonde, G., and N. Wagneur, Evaluation of global numerical weather prediction analyses and forecasts using DMSP special sensor microwave imager retrievals, 1, Satellite retrieval algorithm intercomparison study, *J. Geophys. Res.*, *102*, 1833–1850, 1997.

Ebert, E. E., and J. A. Curry, A parameterization of ice cloud optical properties for use climate models, *J. Geophys. Res.*, *97*, 3831–3836, 1992.

Field, P. R., Bimodal ice spectra in frontal clouds, *Q. J. R. Meteorol. Soc.*, *126*, 379–392, 2000.

Gregory, D., J.-J. Morcrette, C. Jakob, A. C. M. Beljaars, and T. Stockdale, Revision of convection, radiation and cloud schemes in the ECMWF integrated forecasting system, *Q. J. R. Meteorol. Soc.*, *126*, 1685–1710, 2000.

Harrington, J. Y., M. P. Meyers, R. L. Walko, and W. R. Cotton, Parameterization of ice crystal conversion processes in cirrus clouds using double-moment basis functions, Part I, Basic formulation and one-dimensional tests, *J. Atmos. Sci.*, *52*, 4344–4366, 1995.

Harrison, E. F., P. Minnis, B. R. Barkstrom, V. Ramanathan, R. C. Cess, and G. G. Gibson, Seasonal variation of cloud radiative forcing derived from Earth Radiation Budget Experiment, *J. Geophys. Res.*, *95*, 18,687–18,703, 1990.

Kain, J. S., and J. M. Fritsch, Convective parameterization for mesoscale models: The Kain-Fritsch Scheme, in *Meteorological Monograph*, 46, edited by K. Emanuel, pp. 165–170, Am. Meteorol. Soc., Boston, Mass., 1993.

Kessler, E., On the distribution and continuity of water substance in atmospheric circulation, in *Meteorological Monograph 10*, vol. 32, 84 pp., Am. Meteorol. Soc., Boston, Mass., 1969.

Kristjánsson, J. E., J. M. Edwards, and D. L. Mitchell, A new parameterization scheme for the optical properties of ice crystals for use in general circulation models of the atmosphere, *Phys. Chem. Earth B*, *24*, 231–236, 1999.

Lafore, J.-P., et al., The Meso-NH Atmospheric Simulation System. Part I: Adiabatic formulation and control simulations, *Ann. Geophys.*, *16*, 90–109, 1998.

Lin, Y.-L., R. D. Farley, and H. D. Orville, Bulk parameterization of snow field in a cloud model, *J. Clim. Appl. Meteorol.*, *22*, 1065–1092, 1983.

Liu, G., and J. A. Curry, Large-scale cloud features during January 1993 in the North Atlantic Ocean as determined from SSM/I and SSM/T2 observations, *J. Geophys. Res.*, *101*, 7019–7032, 1996.

McFarquhar, G. M., and A. J. Heymsfield, Parameterization of tropical cirrus ice crystal size distributions and implications fo radiative transfer: Results from CEPEX, *J. Atmos. Sci.*, *54*, 2187–2200, 1997.

Mitchell, D. L., S. K. Chai, Y. Liu, A. J. Heymsfield, and Y. Dong, Modeling cirrus clouds, Part I, Treatment of bimodal size spectra and case study analysis, *J. Atmos. Sci.*, *53*, 2952–2966, 1996.

Morcrette, J.-J., Radiation and cloud radiative properties in the European centre for medium range weather forecasts forecasting system, *J. Geophys. Res.*, *96*, 9121–9132, 1991.

Morcrette, J.-J., and Y. Fouquart, On systematic errors in parameterized calculations of longwave radiation transfer, *Q. J. R. Meteorol. Soc.*, *111*, 691–708, 1985.

Ou, S. C., and K.-N. Liou, Ice microphysics and climatic temperature feedback, *Atmos. Res.*, *35*, 127–138, 1995.

Pinty, J.-P., and P. Jabouille, A mixed-phase cloud parameterization for use in a mesoscale non-hydrostatic model: Simulations of a squall line and of orographic precipitations, in *Proceedings of the AMS Conference on Cloud Physics*, pp. 217–220, Everett, Washington, 1998.

Platt, C. M. R., A parameterization of the visible extinction coefficient of ice clouds in terms of the ice/water content, *J. Atmos. Sci.*, *54*, 2083–2098, 1997.

Rasch, P. J., and J. E. Kristjánsson, A comparison of the CCM3 model climate using diagnosed and predicted condensate parameterizations, *J. Climate*, *11*, 1587–1614, 1998.

Redelsperger, J.-L., et al., A GCSS model intercomparison for a tropical sqall line oberved during TOGA-COARE. I: cloud-resolving models, *Q. J. R. Meteorol. Soc.*, *126*, 823–863, 2000.

Roca, R., L. Picon, M. Desbois, H. Le Treut, and J.-J. Morcrette, Direct comparison of METEOSAT water vapor channel data and general circulation model results, *Geophys. Res. Let.*, *24*, 147–150, 1997.

Roca, R., Contribution à l'étude de la vapeur d'eau, de la convection et de leurs interactions dans les Tropiques à l'aide d'observations de satellites et de modèles, Ph.D. thesis, Univ. Paris VII, 2000.

Ryan, B. F., A bulk parameterization of the ice particle size distribution and the optical properties in ice clouds, *J. Atmos. Sci.*, *57*, 1436–1451, 2000.

Smith, E. A., and L. Shi, Surface forcing of the infrared cooling profile over the Tibetan plateau, Part I, Influence of relative longwave radiative heating at high altitude, *J. Atmos. Sci.*, *49*, 805–822, 1992.

Stein, J., E. Richard, J.-P. Lafore, J.-P. Pinty, N. Asencio, and S. Cosma, High-resolution non-hydrostatic simulations of flash-flood episodes with grid-nesting and ice-phase parameterization, *Meteorol. Atmos. Phys.*, *72*, 203–221, 2000.

Stephens, G. L., Radiation profiles in extended water clouds, II, parameterization schemes, *J. Atmos. Sci.*, *35*, 2123–2132, 1978.

Weng, F., and N. C. Grody, Retrieval of cloud liquid water using the special sensor microwave imager (SSM/I), *J. Geophys. Res.*, *99*, 25,535–25,551, 1994.

Wentz, F. J., A well-calibrated ocean algorithm for SSM/I, *J. Geophys. Res.*, *102*, 8703–8718, 1997.

Wentz, F. J., and R. W. Spencer, SSM/I Rain Retrievals within a Unified All-Weather Ocean Algorithm, *J. Atmos. Sci.*, *55*, 1613–1627, 1998.

J.-P. Cammas, J.-P. Chaboureau, P. J. Mascart, and J.-P. Pinty, Laboratoire d'Aérologie, Observatoire Midi-Pyrénées, 14 av. Belin, 31400 Toulouse, France. (camjp@aero.obs-mip.fr; chajp@aero.obs-mip.fr; masp@aero.obs-mip.fr; pinjp@aero.obs-mip.fr)

J.-P. Lafore, CNRM/GMME/MOANA, Météo-France, 42 av. Coriolis, 31057 Toulouse Cedex, France. (Jean-Philippe.Lafore@meteo.fr)